Title: Ocean Acidification and the Permo-Triassic Mass Extinction

Authors: Clarkson, M.O.[1*†]; Kasemann, S.A. [2]; Wood, R.[1]; Lenton, T.M.[3]; Daines, S.J.[3]; Richoz, S.[4]; Ohnemueller, F.[2]; Meixner, A.[2]; Poulton, S.W.[5] and Tipper, E.T.[6]

Affiliations:

[1.] School of Geosciences, University of Edinburgh, West Mains Road, Edinburgh, EH9 3JW, UK

[2.] Faculty of Geosciences and MARUM-Center for Marine Environmental Sciences, University of Bremen, 28334 Bremen, Germany

[3.] College of Life and Environmental Sciences, University of Exeter, Laver Building, North Parks Road, Exeter, EX4 4QE, UK.

[4.] Institute of Earth Sciences, NAWI Graz, University of Graz, Heinrichstraße 26, 8010 Graz, Austria

[5.] School of Earth and Environment, University of Leeds, Leeds, LS2 9JT, UK

[6.] Dept. of Earth Sciences, University of Cambridge, Downing Street, Cambridge, CB2 3EQ, UK

*Correspondence to: matthew.clarkson@otago.ac.nz

[†]Current address: Department of Chemistry, University of Otago, Union Street, Dunedin, 9016, PO Box 56, New Zealand.

Abstract: Ocean acidification triggered by Siberian Trap volcanism was a possible kill mechanism for the Permian Triassic Boundary (PTB) mass extinction, but direct evidence for an acidification event is lacking. We present a high resolution seawater pH record across this interval, using boron isotope data combined with a quantitative modeling approach. In the latest Permian, increased ocean alkalinity, primed the Earth system with a low level of

atmospheric CO_2 and a high ocean buffering capacity. The first phase of extinction was coincident with a slow injection of carbon into the atmosphere and ocean pH remained stable. During the second extinction pulse, however, a rapid and large injection of carbon caused an abrupt acidification event that drove the preferential loss of heavily calcified marine biota.

One Sentence Summary: Ocean acidification caused the second phase of mass extinction in the Permo-Triassic, due to a rapid and large injection of carbon which overwhelmed the buffering capacity of the ocean.

Main Text: The Permian Triassic Boundary (PTB) mass extinction, at ~ 252 million years ago (Ma), represents the most catastrophic loss of biodiversity in geological history, and played a major role in dictating the subsequent evolution of modern ecosystems (*1*). The PTB extinction event spanned ~60,000 years (*2*) and can be resolved into two distinct marine extinction pulses (*3*). The first occurred in the latest Permian [Extinction Pulse 1 (EP1)] and was followed by an interval of temporary recovery before the second pulse (EP2), which occurred in the earliest Triassic. The direct cause of the mass extinction is widely debated with a diverse range of overlapping mechanisms proposed, including widespread water column anoxia (*4*), euxinia (*5*), global warming (*6*) and ocean acidification (*7*).

Models of PTB ocean acidification suggest that a massive and rapid release of CO_2 from Siberian Trap volcanism acidified the ocean (*7*). Indirect evidence for acidification comes from the interpretation of faunal turnover records (*3, 8*), potential dissolution surfaces (*9*), and Ca isotope data (*7*). A rapid input of carbon is also potentially recorded in the negative carbon isotope excursion (CIE) that characterizes the PTB interval (*10, 11*). The interpretation of these records is, however, debated (*12-16*) and is of great importance to understanding the current threat of anthropogenically driven ocean acidification (*11*).

To test the ocean acidification hypothesis we have constructed a proxy record of ocean pH across the PTB, using the boron isotope composition of marine carbonates ($\delta^{11}B_{carb}$) (*17*). We then used a carbon cycle model (*supplementary text*) to explore ocean carbonate chemistry and pH scenarios that are consistent with our $\delta^{11}B$ data and published records of carbon cycle disturbance and environmental conditions. Through this combined geochemical, geological and modelling approach we are able to produce an envelope that encompasses the most realistic range in pH, which then allows us to resolve three distinct chronological phases of carbon cycle perturbation, each with very different environmental consequences for the Late Permian-Early Triassic Earth system.

We analyzed boron and carbon isotope data from two complementary transects in a shallow marine, open water carbonate succession from the United Arab Emirates (U.A.E.), where depositional facies and stable carbon isotope ratio ($\delta^{13}C_{carb}$) are well constrained (*18*). During the PTB interval the U.A.E. formed an expansive carbonate platform that remained connected to the central Neo-Tethyan Ocean (Fig 1A) (*15*). Conodont stratigraphy and the distinct $\delta^{13}C_{carb}$ curve are used to constrain the age model (17).

The run-up to PTB in the Tethys is characterized by two negative $\delta^{13}C$ excursions interrupted by a short-term positive event (*10*). There is no consensus as to the cause of this 'rebound' event and so we instead focus on the broader $\delta^{13}C$ trend. Our $\delta^{13}C$ transect (Fig. 1B) starts in the Changhsingian (Late Permian) with a gradual decreasing trend, interrupted by the first negative shift in $\delta^{13}C$ at EP1 (at 53 m, ~251.96 Ma) (Fig. 1B and 2). This is followed by the minor positive 'rebound' event (at 54 m, ~251.95 Ma) (Fig. 1B and 2) before the minima of the second phase of the negative CIE (58 to 60 m, ~251.92 Ma) (Figs. 1B and 2) that marks the PTB itself. After the CIE minimum, $\delta^{13}C$ gradually increases to ~1.8 per mil (‰) and remains relatively stable during the earliest Triassic and across EP2.

Our boron isotope record shows a different pattern to the carbon isotope excursion. The Boron isotope ratio ($\delta^{11}B$) is persistently low (Fig. 1C) at the start of our record during the late-Changhsingian, with an average of 10.9 ± 0.9‰ (1σ). This is in agreement with $\delta^{11}B$ values (average of 10.6 ± 0.6‰, 1σ) reported for early-Permian brachiopods (*19*). Further up the section (at ~40 m, ~252.04 Ma, Fig. 1C), there is a stepped increase in $\delta^{11}B$ to 15.3±0.8‰ (average ± 2σf), and by implication an increase in ocean pH of ~0.4 to0.5 (Fig. 2). $\delta^{11}B$ values then remain relatively stable, scattering around 14.8± 1.0‰ (1σ) and implying variations within 0.1-0.2 pH units, into the Early Griesbachian (Early Triassic) and hence across EP1 and the period of carbon cycle disturbance (Figs. 1 and 2).

After the $\delta^{13}C$ increase and stabilization (at ~85 m, ~251.88 Ma, Fig. 1), $\delta^{11}B$ begins to decrease rapidly to 8.2±1.2‰ (2σf), implying a sharp drop in pH of ~0.6 to 0.7. The $\delta^{11}B$ minimum is coincident with the interval identified as EP2. This ocean acidification event is short-lived (~10,000 years) and $\delta^{11}B$ values quickly recover toward the more alkaline values evident during EP1 (average of ~14‰).

The initial rise in ocean pH of ~0.4 to 0.5 during the Late Permian (Fig. 2) suggests a large increase in carbonate alkalinity (*20*). We are able to simulate the observed rise in $\delta^{11}B$ and pH through different model combinations of increasing silicate weathering, increased pyrite deposition (*21*), an increase in carbonate weathering, and a decrease in shallow marine carbonate depositional area (*supplementary online text*). Both silicate weathering and pyrite deposition result in a large drop in partial pressure of CO_2 (PCO_2) (and temperature) for a given increase in pH and saturation state (Ω). There is no evidence for a large drop in PCO_2, and independent proxy data indicate only a minor temperature decrease of a few degrees celcius during the Changsingian (*22*), suggesting that these mechanisms alone cannot explain the pH increase (fig. S5). Conversely, an increase in carbonate input or a reduction in rates of

carbonate deposition both result in increases in Ω, with a greater impact on pH per unit decrease in PCO_2 and temperature (fig. S6).

A decrease in carbonate sedimentation is consistent with the decrease in depositional shelf area that occurred because of the second order regression of the Late Permian (*23*). With the added expansion of anoxia into shelf environments (*24*), this would effectively create both bottom-up and top-down pressures to reduce the area of potential carbonate sedimentation. Sea level fall also exposed carbonates to weathering (*23*), which would have further augmented the alkalinity influx. The pH increase event supports the CO_2*Lo* initialization scenario [CO_2 ~3 present atmospheric levels (PAL) , pH ~8, $\delta^{11}B_{SW}$ ~34‰] because the simulated CO_2 and temperature decrease is much reduced and is therefore more consistent with independent proxy data (*22*), as compared with CO_2*Hi* (CO_2 ~10 PAL, pH ~7.5 $\delta^{11}B_{SW}$ ~36.8‰) (Fig. 2D).

Before EP1, $\delta^{13}C_{carb}$ values began to decrease before reaching the minimum of the globally recognized negative CIE at the PTB (Fig. 1). At this time both $\delta^{11}B$ and ocean pH remained stable. Hypotheses to explain the negative CIE require the input of isotopically light carbon, such as from volcanism (*14, 25*) with the assimilation of very light organic carbon from the surrounding host rock (*26*), methane destabilization (*27*), collapse of the biological pump (*15*), and/or a decrease in the burial of terrestrial carbon (*16*). We can simulate the observed drop in $\delta^{13}C_{carb}$, whilst remaining within the uncertainty of the $\delta^{11}B$ data (Fig. 2), by combining a cessation of terrestrial carbon burial with a relatively slow (50,000 years) carbon injection from any of the above sources (fig. S8). A small source of methane (3.2×10^{17} mol C with $\delta^{13}C$ = -50‰) gives the least change in $\delta^{11}B$ and pH, whereas either a larger source of organic carbon (~6.5×10^{17} mol C with $\delta^{13}C$ = -25‰) or a mixture of mantle and lighter carbon sources (~1.3×10^{18} mol C with $\delta^{13}C$ = -12.5‰) are still within the measured uncertainty in $\delta^{11}B$.

This relatively slow addition of carbon minimizes the tendency for a transient decline in surface ocean pH in an ocean that was already primed with a high Ω and hence high buffering capacity from the Late Permian. The global presence of microbial and abiotic carbonate fabrics after EP1 (*28*) are indicative that this high Ω was maintained across the CIE. The carbon injection triggers an increase in PCO_2, temperature and silicate weathering, creating an additional counterbalancing alkalinity flux, which is consistent with independent proxy data (*6*). The alkalinity source may have been further increased through soil loss (*29*), the emplacement of easily-weathered Siberian Trap basalt, or the impact of acid rain (*30*) that would have increased weathering efficiency.

The negative $\delta^{11}B_{carb}$ excursion at 251.88 Ma represents a calculated pH decrease of up to 0.7 pH. This pH decrease coincides with the second pulse of the extinction (Fig. 1), which preferentially affected the heavily calcifying, physiologically un-buffered and sessile organisms (*3*). This was also accompanied by the temporary loss of abiotic and microbial carbonates throughout the Tethys (*31, 32*), suggesting a coeval decrease in Ω. To overwhelm the buffering capacity of the ocean and decrease pH in this way requires a second, more abrupt injection of carbon into the atmosphere, yet remarkably, the acidification event occurs after the decline in $\delta^{13}C$, when $\delta^{13}C$ has rebounded somewhat and is essentially stable (Fig. 1).

Unlike the first carbon injection, the lack of change in $\delta^{13}C$ at this time rules out very ^{13}C-depleted carbon sources, because no counterbalancing strongly ^{13}C-enriched source exists. Instead, it requires a carbon source near ~0‰. A plausible scenario for this is the decarbonation of overlying carbonate host rock, into which the Siberian Traps intruded (*26*) or the direct assimilation of carbonates and evaporites into the melt (*33*). Host carbonates would have had $\delta^{13}C$ ~ +2 to 4‰, which when mixed with mantle carbon (~-5‰), potentially produces a source near 0‰. We can simulate the sharp drop in pH and stable $\delta^{13}C$ values

(Fig. 2) through a large and rapid carbon release of $2x10^{18}$mol C over 10,000 years (fig. S8). This is undoubtedly a massive injection of 24,000 PgC at a rapid rate of 2.4 PgC/yr, but it is physically plausible given existing estimates of the volume of carbonate host sediments subject to contact metamorphism and postulated mechanisms of carbon release (*supplementary text*). This second rapid carbon release produces a sharp rise in PCO_2 to ~20 PAL and warming of ~15˚C, which is consistent with the observation of peak temperatures after EP1 (*22*). Initialization of the carbon cycle model under CO_2*Hi* cannot generate the magnitude of $\delta^{11}B$ drop (Fig. 2A) because the non-linear relation between pH and $\delta^{11}B$ fractionation sets a lower limit of $\delta^{11}B$ at ~10‰ in this case (fig. S3). Thus low initial CO_2 of ~3 PAL in the late Permian (CO_2*Lo*) is more consistent with our data.

An acidification event of ~10,000years is consistent with the modelled timescale required to replenish the ocean with alkalinity, as carbonate deposition is reduced and weathering is increased under higher PCO_2 and global temperatures. Increased silicate weathering rates drive further CO_2 drawdown resulting in stabilization (fig. S7). High global temperature (*6*) and increased silicate weathering are consistent with a sudden increase in both $^{87}Sr/^{86}Sr$ (*34*) and sedimentation rates (*29*) in the Griesbachian.

The PTB was a time of extreme environmental change, and our combined data and modeling approach falsifies several of the mechanisms currently proposed. Although the coincident stresses of anoxia, increasing temperature, and ecosystem restructuring were important during this interval, the $\delta^{11}B$ record strongly suggests that widespread ocean acidification was not a factor in the first phase of the mass extinction, but did drive the second pulse. The carbon release required to drive the observed acidification event must have occurred at a rate comparable with the current anthropogenic perturbation, but exceeds it in expected magnitude. Specifically, the required model perturbation of 24,000 PgC exceeds the ~5000 PgC of conventional fossil fuels and is at the upper end of the range of estimates of

unconventional fossil fuels (such as methane hydrates). We show that such a rapid and large release of carbon is critical to causing the combined synchronous decrease in both pH and saturation state that defines an ocean acidification event (*11*).

References and Notes

1. D. H. Erwin, The Permo-Triassic Extinction. *Nature* **367**, 231-236 (1994).

2. S. D. Burgess, S. A. Bowring, S. Z. Shen, High-precision timeline for Earth's most severe extinction. *Proceedings of the National Academy of Sciences of the United States of America* **111**, 3203-3204 (2014).

3. H. J. Song, P. B. Wignall, J. A. Tong, Y. Hongfu, Two pulses of extinction during the Permian-Triassic crisis. *Nat. Geosci.* **6**, 52-56 (2012).

4. P. B. Wignall, R. J. Twitchett, Oceanic anoxia and the end Permian mass extinction. *Science* **272**, 1155-1158 (1996).

5. K. Grice, C. Q. Cao, G. D. Love, M. E. Bottcher, R. J. Twitchett, E. Grosjean, R. E. Summons, S. C. Turgeon, W. Dunning, Y. G. Jin, Photic zone euxinia during the Permian-Triassic superanoxic event. *Science* **307**, 706-709 (2005); (10.1126/science.1104323).

6. Y. D. Sun, M. M. Joachimski, P. B. Wignall, C. B. Yan, Y. L. Chen, H. S. Jiang, L. N. Wang, X. L. Lai, Lethally Hot Temperatures During the Early Triassic Greenhouse. *Science* **338**, 366-370 (2012); (10.1126/science.1224126).

7. J. L. Payne, A. V. Turchyn, A. Paytan, D. J. DePaolo, D. J. Lehrmann, M. Y. Yu, J. Y. Wei, Calcium isotope constraints on the end-Permian mass extinction. *Proceedings of the National Academy of Sciences of the United States of America* **107**, 8543-8548 (2010); (10.1073/pnas.0914065107).

8. A. H. Knoll, R. K. Barnbach, J. L. Payne, S. Pruss, W. W. Fischer, Paleophysiology and end-Permian mass extinction. *Earth and Planetary Science Letters* **256**, 295-313 (2007); (10.1016/j.epsl.2007.02.018).

9. J. L. Payne, D. J. Lehrmann, D. Follett, M. Seibel, L. R. Kump, A. Riccardi, D. Altiner, H. Sano, J. Wei, Erosional truncation of uppermost Permian shallow-marine carbonates and implications for Permian-Triassic boundary events. *Geol. Soc. Am. Bull.* **119**, 771-784 (2007); (10.1130/b26091.1).

10. C. Korte, H. W. Kozur, Carbon-isotope stratigraphy across the Permian-Triassic boundary: A review. *Journal of Asian Earth Sciences* **39**, 215-235 (2010); (10.1016/j.jseaes.2010.01.005).

11. B. Hönisch, A. Ridgwell, D. N. Schmidt, E. Thomas, S. J. Gibbs, A. Sluijs, R. Zeebe, L. Kump, R. C. Martindale, S. E. Greene, W. Kiessling, J. Ries, J. C. Zachos, D. L. Royer, S. Barker, T. M. Marchitto, Jr., R. Moyer, C. Pelejero, P. Ziveri, G. L. Foster, B. Williams, The Geological Record of Ocean Acidification. *Science* **335**, 1058-1063 (2012); (10.1126/science.1208277).

12. C. L. Blätter, H. C. Jenkyns, L. M. Reynard, G. M. Henderson, Signifcant increases in global weathering during Oceanic Anoxic Events 1a and 2 indicated by calcium isotopes. *Earth and Planetary Science Letters* **309**, 77-88 (2011).

13. P. B. Wignall, S. Kershaw, P. Y. Collin, S. Crasquin-Soleau, Erosional truncation of uppermost Permian shallow-marine carbonates and implications for Permian-Triassic

boundary events: Comment. *Geol. Soc. Am. Bull.* **121**, 954-956 (2009); (10.1130/b26424.1).

14. R. A. Berner, Examination of hypotheses for the Permo-Triassic boundary extinction by carbon cycle modeling. *Proceedings of the National Academy of Sciences of the United States of America* **99**, 4172-4177 (2002); (10.1073/pnas.032095199).

15. M. R. Rampino, K. Caldeira, Major perturbation of ocean chemistry and a 'Strangelove Ocean' after the end-Permian mass extinction. *Terra Nova* **17**, 554-559 (2005); (10.1111/j.1365-3121.2005.00648.x).

16. W. S. Broecker, S. Peacock, An ecologic explanation for the Permo-Triassic carbon and sulfur isotope shifts. *Global Biogeochemical Cycles* **13**, 1167-1172 (1999).

17. Materials and methods are available on Science online

18. M. O. Clarkson, S. Richoz, R. A. Wood, F. Maurer, L. Krystyn, D. J. McGurty, D. Astratti, A new high-resolution delta C-13 record for the Early Triassic: Insights from the Arabian Platform. *Gondwana Research* **24**, 233-242 (2013); (10.1016/j.gr.2012.10.002).

19. M. M. Joachimski, L. Simon, R. van Geldern, C. Lecuyer, Boron isotope geochemistry of Paleozoic brachiopod calcite: Implications for a secular change in the boron isotope geochemistry of seawater over the Phanerozoic. *Geochimica et Cosmochimica Acta* **69**, 4035-4044 (2005); (10.1016/j.gca.2004.11.017).

20. The alternative way to drive an increase in pH would be through a removal of carbon; however this would be evident in the $\delta^{13}C$ record so we can rule it out.

21. Bacterial sulfate reduction (BSR) is a net source of alkalinity if the generated H_2S is buried as pyrite. Pyrite deposition is seen widely in certain settings during the Late Permian to PTB. Further information is provided in the supplementary materials.

22. M. M. Joachimski, X. L. Lai, S. Z. Shen, H. S. Jiang, G. M. Luo, B. Chen, J. Chen, Y. D. Sun, Climate warming in the latest Permian and the Permian-Triassic mass extinction. *Geology* **40**, 195-198 (2012); (Doi 10.1130/G32707.1).

23. H. Yin, H. Jiang, W. Xia, Q. Feng, N. Zhang, J. Shen, The end-Permian regression in South China and its implication on mass extinction. *Earth-Sci. Rev.* **137**, 19-33 (2014); (http://dx.doi.org/10.1016/j.earscirev.2013.06.003).

24. P. B. Wignall, R. J. Twitchett, Extent, duration, and nature of the Permian-Triassic superanoxic event. *Catastrophic Events and Mass Extinctions: Impacts and Beyond*, 395-413 (2002).

25. C. Korte, P. Pande, P. Kalia, H. W. Kozur, M. M. Joachimski, H. Oberhaensli, Massive volcanism at the Permian-Triassic boundary and its impact on the isotopic composition of the ocean and atmosphere. *Journal of Asian Earth Sciences* **37**, 293-311 (2010); (10.1016/j.jseaes.2009.08.012).

26. H. Svensen, S. Planke, A. G. Polozov, N. Schmidbauer, F. Corfu, Y. Y. Podladchikov, B. Jamtveit, Siberian gas venting and the end-Permian environmental crisis. *Earth and Planetary Science Letters* **277**, 490-500 (2009); (10.1016/j.epsl.2008.11.015).

27. E. S. Krull, G. J. Retallack, $\delta^{13}C$ depth profiles from paleosols across the Permian-Triassic boundary: Evidence for methane release. *Geol. Soc. Am. Bull.* **112**, 1459-1472 (2000); (10.1130/0016-7606(2000)112<1459:CDPFPA>2.0.CO;2).

28. A. D. Woods, Assessing Early Triassic Paleoceanographic conditions vias unusual sedimentary fabrics and features. *Earth-Sci. Rev.*, (2013); (http://dx.doi.org/10.1016/j.earscirev.2013.08.015).

29. T. J. Algeo, Z. Q. Chen, M. L. Fraiser, R. J. Twitchett, Terrestrial-marine teleconnections in the collapse and rebuilding of Early Triassic marine ecosystems. *Palaeogeography Palaeoclimatology Palaeoecology* **308**, 1-11 (2011); (10.1016/j.palaeo.2011.01.011).

30. B. A. Black, J. F. Lamarque, C. A. Shields, L. T. Elkins-Tanton, J. T. Kiehl, Acid rain and ozone depletion from pulsed Siberian Traps magmatism. *Geology* **42**, 67-70 (2014); (Doi 10.1130/G34875.1).

31. A. Baud, S. Richoz, S. Pruss, The lower Triassic anachronistic carbonate facies in space and time. *Global and Planetary Change* **55**, 81-89 (2007); (10.1016/j.gloplacha.2006.06.008).

32. S. Richoz, L. Krystyn, A. Baud, R. Brandner, M. Horacek, P. Mohtat-Aghai, Permian-Triassic boundary interval in the Middle East (Iran and N. Oman): Progressive environmental change from detailed carbonate carbon isotope marine curve and sedimentary evolution. *Journal of Asian Earth Sciences* **39**, 236-253 (2010); (10.1016/j.jseaes.2009.12.014).

33. B. A. Black, L. T. Elkins-Tanton, M. C. Rowe, I. U. Peate, Magnitude and consequences of volatile release from the Siberian Traps. *Earth and Planetary Science Letters* **317**, 363-373 (2012); (Doi 10.1016/J.Epsl.2011.12.001).

34. C. Korte, H. W. Kozur, M. M. Joachimski, H. Strauss, J. Veizer, L. Schwark, Carbon, sulfur, oxygen and strontium isotope records, organic geochemistry and biostratigraphy across the Permian/Triassic boundary in Abadeh, Iran. *International Journal of Earth Sciences* **93**, 565-581 (2004); (Doi 10.1007/S00531-004-0406-7).

35. G. M. Stampfli, G. D. Borel, A plate tectonic model for the Paleozoic and Mesozoic constrained by dynamic plate boundaries and restored synthetic oceanic isochrons. *Earth and Planetary Science Letters* **196**, 17-33 (2002); (10.1016/s0012-821x(01)00588-x).

36. S. Z. Shen, C. Q. Cao, H. Zhang, S. A. Bowring, C. M. Henderson, J. L. Payne, V. I. Davydov, B. Chen, D. X. Yuan, Y. C. Zhang, W. Wang, Q. F. Zheng, High-resolution delta C-13(carb) chemostratigraphy from latest Guadalupian through earliest Triassic in South China and Iran. *Earth and Planetary Science Letters* **375**, 156-165 (2013); (Doi 10.1016/J.Epsl.2013.05.020).

37. B. Koehrer, M. Zeller, T. Aigner, M. Poeppelreiter, P. Milroy, H. Forke, S. Al-Kindi, Facies and stratigraphic framework of a Khuff outcrop equivalent: Saiq and Mahil formations, Al Jabal al-Akhdar, Sultanate of Oman. *GeoArabia* **15**, 91-156 (2010).

38. F. Maurer, R. Martini, R. Rettori, H. Hillgartner, S. Cirilli, The geology of Khuff outcrop analogues in the Musandam Peninsula, United Arab Emirates and Oman. *GeoArabia* **14**, 125-158 (2009).

39. S. Kasemann, A. Meixner, A. Rocholl, T. Vennemann, M. Rosner, A. K. Schmitt, M. Wiedenbeck, Boron and oxygen isotope composition of certified reference materials NIST SRM 610/612 and reference materials JB-2 and JR-2. *Geostandards Newsletter-the Journal of Geostandards and Geoanalysis* **25**, 405-416 (2001); (Doi 10.1111/J.1751-908x.2001.Tb00615.X).

40. S. A. Kasemann, D. N. Schmidt, J. Bijma, G. L. Foster, In situ boron isotope analysis in marine carbonates and its application for foraminifera and palaeo-pH. *Chem. Geol.* **260**, 138-147 (2009); (Doi 10.1016/J.Chemgeo.2008.12.015).

41. S. A. Kasemann, C. J. Hawkesworth, A. R. Prave, A. E. Fallick, P. N. Pearson, Boron and calcium isotope composition in Neoproterozoic carbonate rocks from Namibia: evidence for extreme environmental change. *Earth and Planetary Science Letters* **231**, 73-86 (2005); (Doi 10.1016/J.Epsl.2004.12.006).

42. S. A. Kasemann, A. R. Prave, A. E. Fallick, C. J. Hawkesworth, K. H. Hoffmann, Neoproterozoic ice ages, boron isotopes, and ocean acidification: Implications for a snowball Earth. *Geology* **38**, 775-778 (2010); (10.1130/g30851.1).

43. P. B. Wignall, A. Hallam, Facies change and the end-Permian mass extinction in SE Sichuan, China. *Palaios* **11**, 587-596 (1996).

44. L. Breesch, R. Swennen, B. Dewever, F. Roure, B. Vincent, Diagenesis and fluid system evolution in the northern Oman Mountains, United Arab Emirates: Implications for petroleum exploration. *GeoArabia* **16**, 111-148 (2011).

45. G. Paris, A. Bartolini, Y. Donnadieu, V. Beaumont, J. Gaillardet, Investigating boron isotopes in a middle Jurassic micritic sequence: Primary vs. diagenetic signal. *Chem. Geol.* **275**, 117-126 (2010); (10.1016/j.chemgeo.2010.03.013).

46. J. Veizer, D. Ala, K. Azmy, P. Bruckschen, D. Buhl, F. Bruhn, G. A. F. Carden, A. Diener, S. Ebneth, Y. Godderis, T. Jasper, C. Korte, F. Pawellek, O. G. Podlaha, H. Strauss, Sr-87/Sr-86, delta C-13 and delta O-18 evolution of Phanerozoic seawater. *Chem. Geol.* **161**, 59-88 (1999); (Doi 10.1016/S0009-2541(99)00081-9).

47. S. B. Jacobsen, A. J. Kaufman, The Sr, C and O isotopic evolution of Neoproterozoic seawater. *Chem. Geol.* **161**, 37-57 (1999); (Doi 10.1016/S0009-2541(99)00080-7).

48. P. K. Swart, M. J. Kennedy, Does the global stratigraphic reproducibility of delta C-13 in Neoproterozoic carbonates require a marine origin? A Pliocene-Pleistocene comparison. *Geology* **40**, 87-90 (2012); (Doi 10.1130/G32538.1).

49. A. M. Oehlert, P. K. Swart, Interpreting carbonate and organic carbon isotope covariance in the sedimentary record. *Nature Communications* **5**, 7 (2014); (10.1038/ncomms5672).

50. F. Ohnemueller, A. R. Prave, A. E. Fallick, S. A. Kasemann, Ocean acidification in the aftermath of the Marinoan glaciation. *Geology* **42**, 1103-1106 (2014); (10.1130/g35937.1).

51. D. Lemarchand, J. Gaillardet, E. Lewin, C. J. Allegre, The influence of rivers on marine boron isotopes and implications for reconstructing past ocean pH. *Nature* **408**, 951-954 (2000).

52. A. J. Spivack, J. M. Edmond, Boron Isotope Exchange between Seawater and the Oceanic-Crust. *Geochimica et Cosmochimica Acta* **51**, 1033-1043 (1987); (Doi 10.1016/0016-7037(87)90198-0).

53. A. G. Dickson, Thermodynamics of the dissociation of boric-acid in synthetic seawater from 273.15-k to 318.15-k. *Deep-Sea Research Part a-Oceanographic Research Papers* **37**, 755-766 (1990).

54. M. Schobben, M. M. Joachimski, D. Korn, L. Leda, C. Korte, Palaeotethys seawater temperature rise and an intensified hydrological cycle following the end-Permian mass extinction. *Gondwana Research*, (2013); (http://dx.doi.org/10.1016/j.gr.2013.07.019).

55. J. T. Kiehl, C. A. Shields, Climate simulation of the latest Permian: Implications for mass extinction. *Geology* **33**, 757-760 (2005); (Doi 10.1130/G21654.1).

56. R. A. Locarnini, A. V. Mishonov, J. I. Antonov, T. P. Boyer, H. E. Garcia, in *NOAA Atlas NESDIS 61,* S. Levitus, Ed. (U.S. Government Printing Office, Washington, D.C, 2006), vol. 1: Temperature.

57. G. L. Foster, Seawater pH, pCO_2 and [CO_3^{2-}] variations in the Caribbean Sea over the last 130 kyr: A boron isotope and B/Ca study of planktic forminifera. *Earth and Planetary Science Letters* **271**, 254-266 (2008); (10.1016/j.epsl.2008.04.015).

58. N. G. Hemming, B. Honisch, A critical review and recent advances in the boron isotope paleo-pH proxy. *Geochimica et Cosmochimica Acta* **69**, A129-A129 (2005).

59. B. Hönisch, N. G. Hemming, Surface ocean pH response to variations in pCO(2) through two full glacial cycles. *Earth and Planetary Science Letters* **236**, 305-314 (2005); (Doi 10.1016/J.Epsl.2005.04.027).

60. N. G. Hemming, G. N. Hanson, Boron isotopic composition and concentration in modern marine carbonates. *Geochimica et Cosmochimica Acta* **56**, 537-543 (1992).

61. K. Klochko, A. J. Kaufman, W. S. Yao, R. H. Byrne, J. A. Tossell, Experimental measurement of boron isotope fractionation in seawater. *Earth and Planetary Science Letters* **248**, 276-285 (2006); (10.1016/j.epsl.2006.05.034).

62. E. Lewis, D. W. R. Wallace. (Oak Ridge, 1998).

63. J. W. B. Rae, G. L. Foster, D. N. Schmidt, T. Elliott, Boron isotopes and B/Ca in benthic foraminifera: Proxies for the deep ocean carbonate system. *Earth and Planetary Science Letters* **302**, 403-413 (2011).

64. G. L. Foster, P. A. E. Pogge von Strandmann, J. W. B. Rae, Boron and magnesium isotopic composition of seawater. *Geochemistry Geophysics Geosystems* **11**, 10 (2010); (10.1029/2010gc003201).

65. A. Ridgwell, A Mid Mesozoic Revolution in the regulation of ocean chemistry. *Marine Geology* **217**, 339-357 (2005); (Doi 10.1016/J.Margeo.2004.10.036).

66. A. Sanyal, M. Nugent, R. J. Reeder, J. Buma, Seawater pH control on the boron isotopic composition of calcite: Evidence from inorganic calcite precipitation experiments. *Geochimica et Cosmochimica Acta* **64**, 1551-1555 (2000).

67. M. Pagani, D. Lemarchand, A. Spivack, J. Gaillardet, A critical evaluation of the boron isotope-pH proxy: The accuracy of ancient ocean pH estimates. *Geochimica et Cosmochimica Acta* **69**, 953-961 (2005); (Doi 10.1016/J.Gca.2004.07.029).

68. K. Klochko, G. D. Cody, J. A. Tossell, P. Dera, A. J. Kaufman, Re-evaluating boron speciation in biogenic calcite and aragonite using B-11 MAS NMR. *Geochimica et Cosmochimica Acta* **73**, 1890-1900 (2009); (10.1016/j.gca.2009.01.002).

69. R. H. Byrne, W. S. Yao, K. Klochko, J. A. Tossell, A. J. Kaufman, Experimental evaluation of the isotopic exchange equilibrium B-10(OH)(3)+B-11(OH)(4)(-) = B-11(OH)(3)+B-10(OH)(-)(4) in acqueous solution. *Deep-Sea Research Part I-Oceanographic Research Papers* **53**, 684-688 (2006); (10.1016/j.dsr.2006.01.005).

70. J. Payne, L. Kump, Evidence for recurrent Early Triassic massive volcanism from quantitative interpretation of carbon isotope fluctuations. *Earth and Planetary Science Letters* **256**, 264-277 (2007); (10.1016/j.epsl.2007.01.034).

71. A. Ridgwell, R. E. Zeebe, The role of the global carbonate cycle in the regulation and evolution of the Earth system. *Earth and Planetary Science Letters* **234**, 299-315 (2005); (Doi 10.1016/J.Epsl.2005.03.006).

72. R. E. Locklair, A. Lerman, A model of Phanerozoic cycles of carbon and calcium in the global ocean: Evaluation and constraints on ocean chemistry and input fluxes. *Chem. Geol.* **217**, 113-126 (2005); (10.1016/j.chemgeo.2004.12.010).

73. Y. Cui, L. R. Kump, Global warming and the end-Permian extinction event: Proxy and modeling perspectives. *Earth-Science Reviews*, (2014); (http://dx.doi.org/10.1016/j.earscirev.2014.04.007).

74. K. Caldeira, J. F. Kasting, The life span of the biosphere revisited. *Nauture* **360**, 721-723 (1992).

75. J. M. Bergman, T. M. Lenton, A. J. Watson, COPSE: A new model of biogeochemical cycling over Phanerozoic time. *American Journal of Science* **304**, (2004).

76. A. F. Hofmann, K. Soetaert, J. J. Middelburg, F. J. R. Meysman, AquaEnv : An Aquatic Acid–Base Modelling Environment in R. *Aquatic Geochemistry* **16**, 507-546 (2010); (10.1007/s10498-009-9084-1).

77. R. E. Zeebe, P. Westbrooke, A simple model for the $CaCO_3$ saturation state of the ocean: The ‘‘Strangelove,’’ the ‘‘Neritan,’’ and the ‘‘Cretan’’ Ocean. *Geochemistry Geophysics Geosystems* **4**, (2003).

78. J. Zhang, P. D. Quay, D. O. Wilbur, Carbon isotope fractionation during gas-water exchange and dissolution of CO2. *Geochimica et Cosmochimica Acta* **59**, 107-114 (1995).

79. H. D. Holland, in *Treatise on Geochemistry: Vol 6 The oceans and marine geochemistry,* H. D. Holland, K. K. Turekian, Eds. (Elsevier Academic Press, 2003), pp. 583-625.

80. H. Song, J. Tong, T. J. Algeo, H. Song, H. Qiu, Y. Zhu, L. Tian, S. Bates, T. W. Lyons, G. Luo, L. R. Kump, Early Triassic seawater sulfate drawdown. *Geochimica et Cosmochimica Acta* **128**, 95-113 (2014); (10.1016/j.gca.2013.12.009).

81. G. Luo, L. R. Kump, Y. Wang, J. Tong, M. a. Arthur, H. Yang, J. Huang, H. Yin, S. Xie, Isotopic evidence for an anomalously low oceanic sulfate concentration following end-Permian

mass extinction. *Earth and Planetary Science Letters* **300**, 101-111 (2010); (10.1016/j.epsl.2010.09.041).

82. R. E. Zeebe, LOSCAR: Long-term Ocean-atmosphere-Sediment Carbon cycle Reservoir Model v2.0.4. *Geoscientific Model Development* **5**, 149-166 (2012); (10.5194/gmd-5-149-2012).

83. S. Ben-Yaakov, M. B. Goldhaber, The influence of sea water composition on the apparent constants of the carbonate system. *Deep Sea Research and Oceanographic Abstracts* **20**, 87-99 (1973); (10.1016/0011-7471(73)90044-2).

84. Y. Cui, L. R. Kump, A. Ridgwell, Initial assessment of the carbon emission rate and climatic consequences during the end-Permian mass extinction. *Palaeogeography Palaeoclimatology Palaeoecology* **389**, 128-136 (2013).

85. T. J. Algeo, K. Kuwahara, H. Sano, S. Bates, T. Lyons, E. Elswick, L. Hinnov, B. Ellwood, J. Moser, J. B. Maynard, Spatial variation in sediment fluxes, redox conditions, and productivity in the Permian–Triassic Panthalassic Ocean. *Palaeogeography, Palaeoclimatology, Palaeoecology* **308**, 65-83 (2011); (10.1016/j.palaeo.2010.07.007).

86. T. J. Algeo, R. J. Twitchett, Anomalous Early Triassic sediment fluxes due to elevated weathering rates and their biological consequences. *Geology* **38**, 1023-1026 (2010); (10.1130/g31203.1).

87. G. A. Brennecka, A. D. Herrmann, T. J. Algeo, A. D. Anbar, Rapid expansion of oceanic anoxia immediately before the end-Permian mass extinction. *Proceedings of the National Academy of Sciences of the United States of America* **108**, 17631-17634 (2011); (10.1073/pnas.1106039108).

88. S. E. Grasby, B. Beauchamp, Latest Permian to Early Triassic basin-to-shelf anoxia in the Sverdrup Basin, Arctic Canada. *Chem. Geol.* **264**, 232-246 (2009); (Doi 10.1016/J.Chemgeo.2009.03.009).

89. C. Winguth, A. M. E. Winguth, Simulating Permian-Triassic oceanic anoxia distribution: Implications for species extinction and recovery. *Geology* **40**, 127-130 (2012); (10.1130/g32453.1).

90. T. J. Algeo, C. M. Henderson, J. N. Tong, Q. L. Feng, H. F. Yin, R. V. Tyson, Plankton and productivity during the Permian-Triassic boundary crisis: An analysis of organic carbon fluxes. *Global and Planetary Change* **105**, 52-67 (2013); (Doi 10.1016/J.Gloplacha.2012.02.008).

91. E. Tziperman, I. Halevy, D. T. Johnston, A. H. Knoll, D. P. Schrag, Biologically induced initiation of Neoproterozoic snowball-Earth events. *Proceedings of the National Academy of Sciences of the United States of America*, 1-6 (2011); (10.1073/pnas.1016361108).

.

92. G. Luo, Y. Wang, K. Grice, S. Kershaw, T. J. Algeo, X. Ruan, H. Yang, C. Jia, S. Xie, Microbial–algal community changes during the latest Permian ecological crisis: Evidence from lipid biomarkers at Cili, South China. *Global and Planetary Change* **105**, 36-51 (2013); (10.1016/j.gloplacha.2012.11.015).

93. K. M. Meyer, M. Yu, A. B. Jost, B. M. Kelley, J. L. Payne, $\delta^{13}C$ evidence that high primary productivity delayed recovery from end-Permian mass extinction. *Earth and Planetary Science Letters* **302**, 378-384 (2011); (10.1016/j.epsl.2010.12.033).

94. H. J. Song, J. N. Tong, Y. L. Xiong, D. Y. Sun, L. Tian, H. Y. Song, The large increase of δ13C(carb)-depth gradient and the end-Permian mass extinction. *Sci. China-Earth Sci.* **55**, 1101-1109 (2012); (10.1007/s11430-012-4416-1).

95. D. E. Ogden, N. H. Sleep, Explosive eruption of coal and basalt and the end-Permian mass extinction. *Proceedings of the National Academy of Sciences of the United States of America* **109**, 59-62 (2012); (10.1073/pnas.1118675109).

96. M. K. Reichow, A. D. Saunders, R. V. White, M. S. Pringle, A. I. Al'Mukhamedov, A. I. Medvedev, N. P. Kirda, Ar-40/Ar-39 dates from the West Siberian Basin: Siberian flood basalt province doubled. *Science* **296**, 1846-1849 (2002).

97. M. B. Harfoot, J. a. Pyle, D. J. Beerling, End-Permian ozone shield unaffected by oceanic hydrogen sulphide and methane releases. *Nat. Geosci.* **1**, 247-252 (2008); (10.1038/ngeo154).

98. C. Ganino, N. T. Arndt, Climate changes caused by degassing of sediments during the emplacement of large igneous provinces. *Geology* **37**, 323-326 (2009); (10.1130/G25325A.1).

Acknowledgements: MOC acknowledges funding from the Edinburgh University Principal's Career Development Scholarship, the International Centre for Carbonate Reservoirs and The Marsden Fund (U001314). RW, TL and SWP acknowledge support from the Natural Environment Research Council (NERC) through the 'Co-evolution of Life and the Planet' scheme (NE/I005978). TL and SD were supported by the Leverhulme Trust (RPG-2013-106). SK and AM acknowledge support from the German Research Foundation (Deutsche Forschungsgemeinschaft Major Research Instrumentation Program). This is a contribution to IGCP 572 with SR sponsored for fieldwork by the Austrian National Committee (Austrian Academy of Sciences) for the International Geoscience Programme (IGCP). We are grateful to R. Newton and A. Thomas for helpful discussions, L. Krystyn for field assistance, F. Maurer for providing photomicrographs, and B. Mills for assisting with model studies. Data are available online in the supplementary materials and at www.pangaea.de

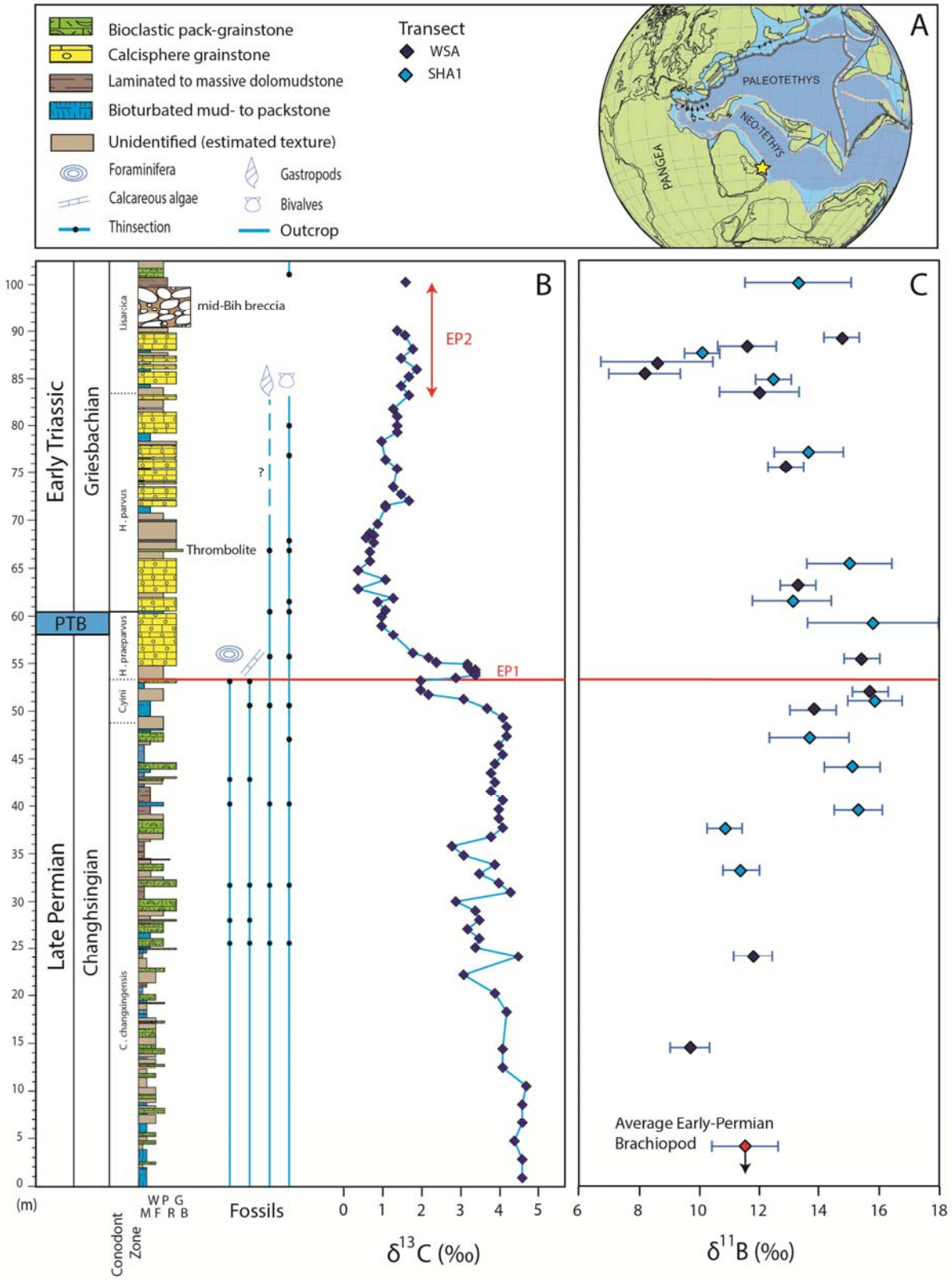

Fig. 1. Site locality and high resolution carbon and boron isotope data. **(A)** Paleogeographic reconstruction for the Late Permian showing the studied section Wadi Bih, in the Musandam

Mountains of U.A.E. that formed an extensive carbonate platform in the Neo-Tethyan Ocean. Modified from (*35*). **(B)** Shallow water $\delta^{13}C$ record (*18*). **(C)** Boron isotope ($\delta^{11}B$) record (propagated uncertainty given as $2\sigma f$) and average Early Permian brachiopod value (n=5) (*19*). See **(A)** for lithology, biota and transect key. Only *Hindeodus parvus* has been found so far in this section and the conodont zones with dashed line are identified from the $\delta^{13}C$ record (*36-38*).

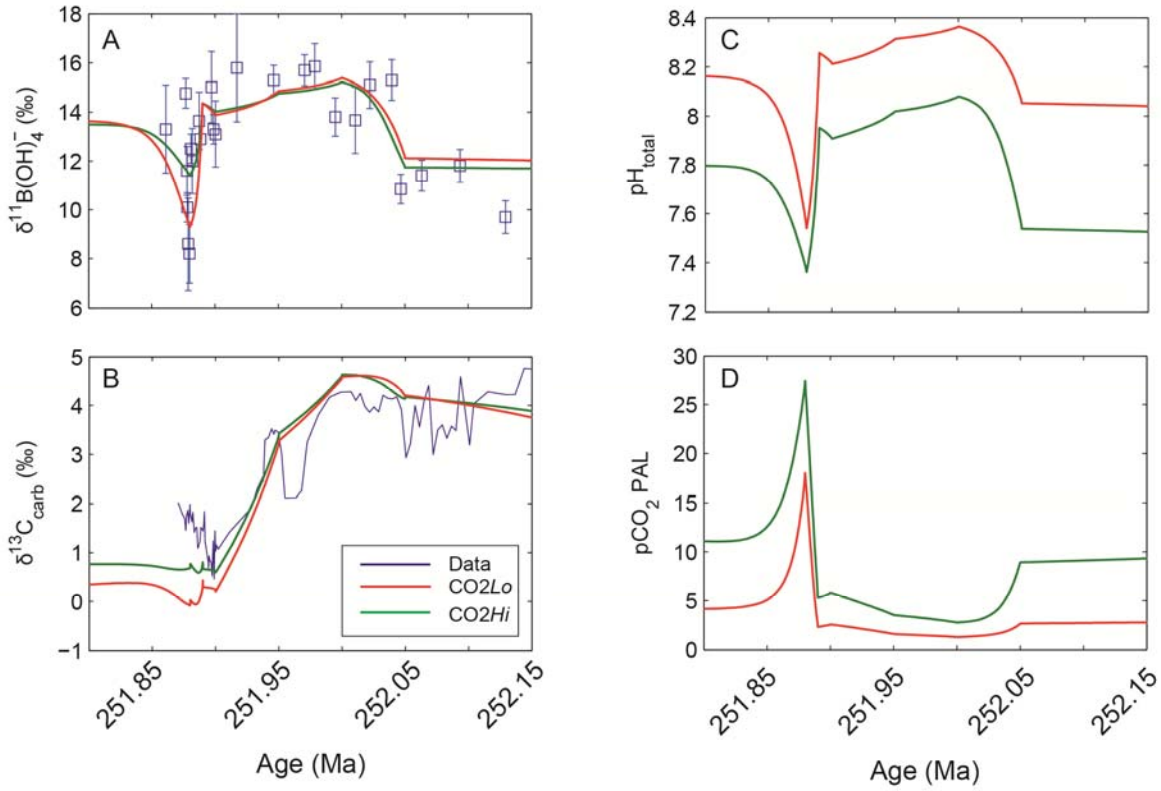

Fig. 2. Model results of carbon cycle parameters for the two end-member CO_2 scenarios; CO_2*Hi* and CO_2*Lo* (17). **(A)** Model reproduced $\delta^{11}B$ vs data. **(B)** Modelled $\delta^{13}C$ vs data. **(C)** Modelled pH envelope incorporating uncertainty of seawater B isotope composition ($\delta^{11}B_{SW}$) and dynamic temperatures. **(D)** Calculated atmospheric CO_2.

Materials and Methods

1.1 Sample Section

Carbonate samples were obtained from a shallow-marine platform section at Wadi Bih on the Musandam Peninsula, United Arab Emirates (U.A.E.). GPS co-ordinate for main transect in Wadi Shahha are N 025° 50′ 31.7″, E 056° 06′ 41.7″. This is a near-continuous and exclusively shallow marine carbonate succession from the late Permian and entire Early Triassic that allows analysis of a high-resolution signature in the absence of significant depth-dependent or lithological controls (*18*). Late Permian facies are predominantly intertidal mud-and-wackestones and open lagoon wackestones, occasional windward and leeward shoals of bioclastic pack-and-grainstones (*38*). The PTB and Early Triassic are regionally represented by ooidal grainstones, calcisphere grainstones and a thrombolite horizon (*18, 38*). Samples were taken from two transects Wadi Shahha (WSA) and Sha (SHA1), ~1000 m apart. Facies are laterally continuous and carbon isotopes were used to ensure careful integration of the two datasets. For this study, we have analyzed 25 carbonate samples in total, taken in approximately 1 to 10 m scale intervals and covering a total thickness of 102m (including a tectonic breccia), starting in the mid-Changhsingian (Permian), going up into the mid-Griesbachian (Triassic) and bracketing the complete Permian Triassic Boundary (PTB) extinction event (Table S1).

1.2 Age Model

The age model for this study was based on the most recent findings of (*2*) (see Table S1). The age tie points are 252.10 Ma for 20 m (Fig. 1) thought to be equivalent to Bed 22 in Meishan from the $\delta^{13}C$ record; 252.00 Ma for the decline in $\delta^{13}C$ at 49 m and 251.90 Ma for the first occurrence of *Hindeodus parvus* at 61m. EP2 is known to occur at the end of the *Isarcicella staeschi* zone, Bed 28 Meishan (*3*), a conodont that is not recorded in the Neo-Tethys but is equivalent to the carbon isotope rise between the *Hindeodus parvus* and *Isarcicella isarcica* zones. In Wadi Bih we see the loss of gastropods and bivalves at this point (*18*), however the full resolution of the second extinction phase has not been confirmed at this locality. Therefore we identify a 10 m interval for EP2. In order to complete the age model we set the mid-point of EP2 as 251.88 Ma based on the absolute age for EP2 in Meishan (*2*).

1.3 Analytical methods

Carbon and oxygen isotope ratios were determined at the University of Edinburgh , University of Graz and University of Bremen using the preparation technique and measurement routine as detailed in (*18*). All carbonate isotopic values are quoted in the conventional δ per mil (‰) notation relative to VPDB. Calibration to international reference material was through NBS 19 and the reproducibility of replicate analyses for reference material, standards (in-house) and carbonate samples was better than ±0.05 ‰ for $\delta^{13}C$ and ±0.1 ‰ for $\delta^{18}O$ at one standard deviation. For a detailed discussion of the C and O isotopic data see (*18*).

Boron isotope ratios were determined in the isotope geochemistry laboratory at the University of Bremen (Department of Geosciences and MARUM-Center for Marine Environmental Sciences) using a ThermoFisher Scientific TRITON Plus Thermal Ionization Mass Spectrometer. The $n(^{11}B)/n(^{10}B)$ measurements were performed using negative thermal ionization mass spectrometry (N-TIMS) following the method detailed in (*39*). For analyses, 10 mg of the sample powder was dissolved in 100 µl 1 N HCl for 24 h at 20°C and subsequently centrifuged. 1 µl boron-free seawater emitter (*39*) together with 10 µl of the sample solution containing ~1 ng B were placed and dried on a degassed Re single filament. Analyses were carried out at filament temperatures of 970°-1050°C. Boron isotopes were registered as BO_2^- complexes on masses 42 and 43, and measurements were carried out at ion beam intensity of ~ 10 pA on mass 43. Each sample measurement involved up to 200 blocks with 10 cycles each, taking about 2 hours of data acquisition. B isotope ratios are given relative to NIST SRM 951 in the conventional $\delta^{11}B$ (‰) notation. The external reproducibility of the certified reference material NIST SRM 951 showed an $n(^{11}B)/n(^{10}B)$ ratio of 4.0065±0.0017 (2σ = 0.42‰, n=23) over a period of 6 month of sample analyses. The long term (18 month) reproducibility is 4.0066±0.0018 (2σ = 0.44‰, n=58). The $n(^{11}B)/n(^{10}B)$ ratio of the reference material for each analytical session was reproduced better than 0.6‰ (2σ). In addition to the NIST material, the standard material M93-TB-FC-1, a *Porites* coral with a published value of 24.8±0.4‰ ($2\sigma_{mean}$), as determined by different

multicollector techniques (*40*) was also regularly analyzed. The coral replicates gave $\delta^{11}B$ values of 24.1±0.7‰ (2σ, n=16). Each sample solution was as a minimum run in full duplicate and the uncertainty of the reference material was propagated into the external uncertainty (2σ) on the isotope ratio of the sample (2σf; Table S1). For further information on the preparation and analytical methods see *(39, 41)*.

Element concentrations (Table S2) were determined by inductively coupled plasma optical emission spectrometry (ICP-OES) on an Agilent 700 at the inorganic geochemistry laboratory, University of Bremen (MARUM-Center for Marine Environmental Sciences). All samples were prepared by dissolving ~40 mg of carbonate powder in 2 ml of 0.5 N HCl. High Purity Standards certified multi element standards were used for element-specific instrumental calibration. Three replicates were measured and the relative analytical uncertainties were better than 4% (2σr) for all element concentration determinations expect for boron, aluminum (both ~ 20%) and barium (~ 10%).

Supplementary Text

2. Sample Selection

A critical issue in using the B isotope composition of Permo-Triassic carbonate rocks for reconstruction of ocean pH is the potential overprinting of the original isotope signal via alteration. To obtain high-quality samples in which primary B isotope signals are still preserved, we applied the sample selection procedures successfully used on Neoproterozoic carbonate rocks to reconstruct Cryogenian and Ediacaran ocean pH variation *(41, 42)*. In brief, samples selected for isotope analyses were screened macroscopic (in the field), microscopic (scanning electron microscope) and geochemically (carbon and oxygen isotopes), and selected because of their uniformity in texture, absence of late stage secondary alteration and no correlation between carbon and oxygen isotopic signatures (Figs. S1 and S2).

The PTB interval itself was thought to occur in a regional cross-bedded ooid grainstone, however, reconsideration of published thin-section images (*38*) (Fig. S1 samples from WSA transect, 0611300847 and 0611181243) demonstrate these are in fact microspheres (a.k.a calcispheres). This fabric is unusual for the Phanerozoic but appears to represent supersaturated conditions and these are thought to be primary spar precipitates (*43*).

In order to gain the highest potential for recording primary isotope signatures, we microdrilled areas of pure micrite from micritc mudstones and micritised calcisphere grainstones. 3 samples were bioclastic packstones, however again areas of pure micrite were sampled. There was no micro-optical evidence for veining, fracturing, clay minerals or bioclastic material. Samples containing evidence of late stage secondary alteration or recrystallization, i.e. any spar/microspar, were discarded. The low availability of bioclastic material in this interval, due to the extinction, argues against the potential of trends being caused by vital effects. In particular the calcisphere grainstones of the PTB interval are classed as an abiotic carbonate that provides an excellent opportunity to record seawater $\delta^{11}B$ in the absence of vital effects.

The WSA1 $\delta^{13}C$ and $\delta^{18}O$ data were originally analyzed for (*18*) and used for the reference curve in Fig. 2. Sample material for the B isotope and elemental analyses was re-drilled from the same sample chips in close proximity to the carbon/oxygen sample points. All isotope (C, O, B) and elemental data for the SHA1 sample set were analyzed from the same sample powder.

2.1 Diagenetic Influences

Diagenetic alteration in ancient carbonates is always a concern when arguing for preservation of a primary environmental signal, and any geochemical data should be scrutinized within a comprehensive assessment of diagenesis. The PTB interval grainstone is composed of microspheres (a.k.a calcispheres). Microspheres are micritized and cemented with coarse equant spar cement (Fig. S1). The lack of compaction of the microspheres suggests that the spar cement was extremely early and probably syn-sedimentary. This is a feature of other grainstones throughout this interval (WSA transect, sample 0611301104). Critically the presence of such well cemented fabrics in the grainstones of this interval would have prevented later stage fluid migration, and hence any late stage dolomitization. The total negative boron isotope excursion at EP2 is recorded across a number of fabrics and facies, including micrite and the early cemented grainstones.

Dolomitization in the Wadi Bih section is observed (*18*), and occurred in two phases where the first phase was fabric retentive syn-sedimentary dolomitization. The second phase of dolomitization leads to the recrystallization of facies where near depositional porosity and permeability had been maintained, i.e. preferentially in non-cemented grainstones. Neither of these phases is classed as deep burial dolomitization (as confirmed by petrography in Fig. S1 and $\delta^{18}O$ data, Table S1). In the Musandam Peninsula the impact of dolomitization on carbon and oxygen isotopes can be seen only in the close proximity to regional faults that provided high permeability pathways for late burial dolomitizing fluids (*44*), which were avoided for this study. One of our samples (SHA1/11) is anomalous and shows a lower $\delta^{18}O$ of -7.36‰ (Fig. S2B), however this sample replicates the boron isotopic signature of the equivalent WSA sample (WSA 21) within uncertainty.

Post-depositional alteration, especially meteoric diagenesis and recrystallization, is assumed to decrease the isotopic composition of oxygen, boron and carbon isotopes (*45, 46*). Our selected carbonate samples show the distinct carbon isotope trend found at every PTB section globally and $\delta^{18}O$ values ranging between -0.5 and -4 with only one sample showing -7.36‰, indicating no significant deep burial alteration. All carbon and oxygen isotope data are given in Table S1. No statistically significant correlation between carbon, oxygen and boron isotope data can be observed in our data. In addition, there is no correlation between boron concentration and boron isotope data indicating no depletion of boron amount content and ^{11}B by diagenetic recrystallization (Fig. S2A).

Diagenetic effects were also checked with geochemical tests for selected trace element analyses; all elemental data are given in Table S2. Diagenetic alteration was explored via Mn/Sr, which is often used as a geochemical indicator of alteration and meteoric diagenesis in ancient carbonates (*47*). While low Mn/Sr has been found in ancient carbonates where there is clear optical evidence for recrystallization (*42*), high Mn/Sr may indicate carbonate precipitation from anoxic waters. In the selected samples, Mn concentration is < 100 μg g^{-1}, Sr concentration ranges from 48 to 106 μg g^{-1}, and the Mn/Sr ratio is low (< 2), so suggesting no influence of meteoric fluids. The boron concentration for the carbonate rocks is, on average, 1.4 μg g^{-1} and ranges between 0.5 and 2.5 μg g^{-1}. Potential analyses of disseminated detrital material in the carbonates was also checked through elevated Al, Si and Ba concentrations and showed either no or only minor dissemination of clay. No statistically significant correlation between boron and elemental (Al, Ba, Ca, Fe, Mg, Mn, P, S, Si, Sr) data can be observed in our data.

The replication of the $\delta^{11}B$ across two complementary transects further support the preservation of a primary seawater isotope signature as late stage dolomitization is expected to be highly laterally variable and disrupt the smooth trends seen in the data.

2.1.1 Potential influence of meteoric diagenesis

Some studies on negative $\delta^{13}C$ excursions in marine carbonates (*48, 49*) have made a case for the potential of meteoritic alteration of Neoproterozoic to Pliocene carbonate platforms; the same could be argued for the negative $\delta^{11}B$ excursions.

The distinct carbon isotope trend is found at every PTB section globally. It is difficult to explain this by any diagenetic processes as these are inherently local. The hypothesis that large and systematic negative shifts in the $\delta^{13}C$ values can be produced by periods of meteoric alteration in response to sea-level fall (*48, 49*) indeed only applies in certain settings and sea-level histories. If the hypothesis were correct and could explain the $\delta^{13}C$ record for the PTB we would see a coupled response of $\delta^{11}B$ where the influx of meteoric waters would alter both geochemical signals. We do not see, however, a $\delta^{13}C$ excursion over the EP2 horizon.

If we accept that the negative boron isotope excursion is a diagenetic feature, than we also have to accept, that the diagenetic front (i) only affected 4 meters of the transect, (ii) is locally coincident with the extinction phase 2, (iii) cuts across different facies, and finally (iv) did not affect the C and O isotope composition of the same rocks. Such a scenario is highly unlikely.

The negative boron isotope excursion in the early Triassic is only one of three distinct boron isotope features across the PTB which have led us to the hypothesis of three key and chronological changes in the Earth System. If the other two patterns were also the result of diagenetic fronts passing across the transects then we have to evoke three discrete fronts, with each placing a different force on the B isotope ratio and all equally incapable of changing $\delta^{13}C$ and $\delta^{18}O$. Unlike the third front at EP2, the first front must have been capable of producing a positive shift in $\delta^{11}B$ without changing $\delta^{13}C$ and $\delta^{18}O$. A hydrothermal fluid would be able to produce such a positive shift in $\delta^{11}B$, but we have no indications for hydrothermal alteration and such a fluid would certainly also affect $\delta^{13}C$ and $\delta^{18}O$. The second front must have cut across EP1, resetting the B isotope data to nearly identical values, and again would not affect $\delta^{13}C$ and $\delta^{18}O$; we are not aware of any potential mechanism for this.

2.1.2 Summary

1. We have replicated the boron isotope pattern in two sections 1 km apart, which allows consideration of the lateral consistency of the geochemical signature. These sections show a remarkably consistent signal and a synchronous excursion event, so reinforcing our argument that we indeed have identified a primary signal (see Fig. 2, blue and black symbols).

2. The boron isotope pattern cuts across primary lithological boundaries, including micritic carbonates, grainstones, and intervals with calcispheres (Fig. 2). Our $\delta^{11}B$ trends are therefore both facies and fabric independent, as would be expected if our signal was primary. This would not be the case if the depositional signature had been substantially altered via diagenesis.

3. Calcispheres are abiotic and hence should also record $\delta^{11}B$ in the absence of vital effects. The lack of biomineralizers after the extinction event minimises the possibility of a biotic source for the micrite component.

4. To extent the evaluation of diagenesis, thin section images are provided to argue for retention of a primary signal in these samples. Through petrographic analysis (Fig. S1) we show that these samples were subject to only very early, probably syn-sedimentary diagenesis and early dolomitization. Where this has been the case in other ancient carbonates, this has allowed the preservation of original depositional textures. The calcispheres show no evidence for severe compaction but some grains are touching. They are cemented by coarse equant early marine spar cement that would prevent any later stage dolomitization by pore fluids as the porosity of the facies is fully occluded. Micritic samples have previously been used for $\delta^{11}B$ analysis (*41, 42, 45, 50*) and have successfully been used to record clear trends in $\delta^{11}B$. We have used the same sampling approach, targeting abiotic carbonate and homogenous micrite where veins, heavily recrystallized, and bioclastic material have been avoided.

5. Meteoric diagenesis can be detected by distinct, non-luminescent cements, and also in some cases by a negative carbon isotope excursion. There is no evidence in thin-section for these distinct (vadose or phreatic) cements in the grainstones (i.e. no evidence for patchy distribution of cements, meniscus cements, drusy spar, coarse dolomite overgrowths, and incomplete pore fills etc). $\delta^{18}O$ and $\delta^{13}C$ do not show any correlation (Fig. S2), as would be expected by meteoric alteration or late stage dolomitization.

6. Dolomitization is indeed present in the outcrop but has not affected the carbon and oxygen isotope signatures of the majority of samples. One sample shows a more negative $\delta^{18}O$ value of -7.36, but shows excellent replication of $\delta^{11}B$ (Fig. S2B). Later stage dolomitization is an extremely heterogeneous process and due to the low porosity of these micritic and grainstone samples they are unlikely to have undergone later stage dolomitization. Indeed, no replacement late dolomite crystals are seen in these samples. Dolomitization per se does not appear to disrupt the $\delta^{11}B$ signature, as shown by the published data (*41, 42, 50*) from the dolomitic cap carbonates that formed in the Cryogenian and Ediacaran after the 'Snowball' Earths.

3. Support for a primary boron isotope signature

3.1 Published $\delta^{11}B$ data

So far, $\delta^{11}B$ data for Triassic carbonates have not been published and only limited $\delta^{11}B$ data, based on low-Mg calcite brachiopod calcite from Oman (Saiwan Fm.), are available for the Permian (Late Sakmarian). Keeping in mind the modern residence time of boron (τ~14 to 20 Ma (*51, 52*), it is important to note that the range in $\delta^{11}B$ values (10.9±0.9‰ (1σ, n=4), 252.05-252.15 Ma, mid-Changhsingian) overlap with the range in $\delta^{11}B$ values between 10.1 and 11.7‰ of the 285 Ma old brachiopod carbonates (Fig. 1, average 10.6±0.‰, 1σ, n=5, (*19*)), which support the primary nature of our boron isotope data.

3.2 Environmental controls on the boron isotope composition

The speciation of boron in seawater is predominantly pH dependent with minor controls from temperature, salinity and pressure (*53*). In our model we consider a dynamic temperature effect on pK_B to calculate the pH of the seawater from the boron isotope composition preserved in Permo-Triassic carbonate (see SM 4 and 5) however below we

evaluate geological evidence to consider whether these variables could drive the trends seen in our data.

3.2.1 Temperature

Oxygen isotope data preserved in conodont apatite and low-Mg calcite brachiopods from Permian-Triassic sections in Iran document tropical sea surface temperatures (SST) of 27–33°C during the Changhsingian with a negative shift in $\delta^{18}O$ starting at the extinction horizon, translating into a warming of SSTs to well over 35°C in the mid-Griesbachian (*54*). The results are consistent with SSTs of the South Chinese sections, where a rapid increase in seawater temperature from about 25° to 36°C across the Permian-Triassic section was proposed based on conodont apatite (*6*). Since the dissociation constant of boric acid (pK_B) decreases with increasing temperature (*53*), the proposed increase in SST could drive an increase in the B isotope composition of the carbonates precipitated at the time of global warming and imply an increase in ocean pH, even if ocean pH stayed stable. Using the pK_B data from (*53*), the potential increase in SST at a given pH of 8 would drive an increase in $\delta^{11}B$ of the carbonates by 2‰ and generate an artificial increase of < 0.2 pH units. Consequently, it could be argued that our calculated pH variations are in essence the result of an increase in sea surface temperatures. However, the oxygen isotope pattern (*54*) shows a continuous increase in temperatures across the Permian-Triassic boundary and a thermal maximum in the mid-Griesbachian (~251.85 Ma). Instead our data show a sharp increase in $\delta^{11}B$ and ocean pH in the Late Permian, well before the increase in temperatures at EP1. The slight variability in $\delta^{11}B$ above the PTB, however, could be driven by temperature variations.

3.2.2 Salinity

Similar to temperature, the pK_B is sensitive to salinity and increases with decreasing salinity (*53*). To drive significant salinity-associated isotope variations across the Permo-Triassic boundary, drastic changes in salinity (e.g. down to 25 psu compared to 35 psu) would be necessary. However, even if modelled sea surface salinity values for the late Permian indicate generally more saline conditions than present day (*55*), sea surface salinity values for e.g. Iran and South China still range between 34 and 35 psu (*54*) and will not have a significant effect on our pH calculation. These samples come from an exclusively shallow water environment far from any freshwater input, and so decreases in salinity would not affect our pH interpretations. The depositional environment here ranges between open water ooid shoals to open and restricted lagoon settings, which results in cyclic deposition on the scale of 5m. A shift toward more restricted settings could drive increases in salinity that would affect the $\delta^{11}B$ record; however, these depositional cycles are not on the same scale as the secular trends seen in $\delta^{11}B$.

3.2.3 Water Depth

Permo-Triassic seawater pH values have been reconstructed assuming carbonate precipitation at sea surface conditions. Modern bathymetric pH and temperature profiles from the tropics show that pH can decrease by up to ~0.2 units and temperature can drop by 15°C in the first 300 m (*56*). Thus the B isotope composition of carbonates precipitated at greater water depths would be more negative compared to surface precipitates. This potential depth

effect is thought to be of minimal influence to the Wadi Bih carbonates due to the exclusively shallow marine (subtidal to intertidal) nature of the succession.

Consequently, uncertainties in the $\delta^{11}B$-ocean pH relationship potentially introduced by changes in temperature, salinity, bathymetry or biofacies would not be able to produce the observed B isotope pattern with the sharp increase in the mid-Changhsingian (~252.04 Ma) and the temporary decrease in the mid-Griesbachian (~251.88 Ma), but would be capable of explaining some of the slight variations across the PTB.

4. Boron-pH calculations

The boron isotope composition of marine carbonates is used to reconstruct seawater pH values and atmospheric pCO_2 concentrations (e.g. *57, 58, 59*). The application of the B isotope system as a proxy for ocean pH is based on the observation that the fractionation factor for isotope exchange between the two different speciation of boron ($B(OH)_3$ and $B(OH)_4^-$) is pH sensitive and produces significant and traceable changes in the isotopic composition of carbonates (e.g. *60*) .

The carbonate-associated boron isotopic composition $\delta^{11}B_{carb}$ is assumed to be equal to that of seawater $B(OH)_4^-$. The isotopic composition of the two boron species $B(OH)_4^-$ and $B(OH)_3$ is determined by the isotopic fractionation factor $\alpha_{B3\text{-}B4} = 1.0272$ ((*61*), the speciation (a strong function of pH, with smaller dependencies on temperature, pressure and salinity), and the overall isotopic composition of seawater $\delta^{11}B_{sw.}$ The relationship between pH and $\delta^{11}B_{carb}$ is given by:

$$pH = pK_B - \log\left[- \frac{\delta^{11}B_{SW} - \delta^{11}B_{carb}}{\delta^{11}B_{SW} - \alpha_{B3\text{-}B4} \cdot \delta^{11}B_{carb} - 1000 \cdot (\alpha_{B3\text{-}B4} - 1)} \right]$$

where the effective dissociation constant pK_B includes the temperature, pressure and salinity dependence. We dynamically calculate pK_B using CO2SYS-MATLAB v1.1 (*62*) (detailed in SM 5), which is consistent with the calculation and constants used by (*63*).

A prerequisite for reconstruction of past ocean pH values via B isotope data is the knowledge of the primary B isotope composition $\delta^{11}B_{SW}$ of the ambient seawater. The B isotope composition of modern seawater is regarded as being homogeneous with a $\delta^{11}B$ value of 39.6‰ (*64*). However, recent work on Precambrian to Phanerozoic carbonates and evaporites has shown that the B isotope composition of seawater was highly variable in the geological past (*19, 42, 45*) driven mainly by variations in the global boron budget during Earth history (*19*), exceeding the residence time of B in seawater. Permo-Triassic seawater have been calculated based on changes in processes controlling the oceanic boron budget, e.g. oceanic crust production rate and continental boron flux (*19*) and suggests $\delta^{11}B_{SW}$ values of ~38‰ for the early Permian (285 Ma, Late Sakmarian) and ~34‰ just before the PTB (*19*).

Given this uncertainty in $\delta^{11}B_{SW}$, we consider a range of values, determined by the overall consistency of the $\delta^{11}B_{carb}$ data with model-derived constraints on the seawater carbonate chemistry and hence pH, resulting in an envelope for the pH calculation. The model scenarios encompass the range of previous estimates for background Early Permian conditions(*65*), which suggest either high pCO_2 with lower pH (CO_2*Hi:* ~10 PAL, pH ~7.5), or low pCO_2 with higher pH (CO_2*Lo:* ~3 PAL, pH ~8). In our model we consider these two scenarios with corresponding seawater boron isotopic composition ($\delta^{11}B_{SW} = 34$‰ and 36.8‰) required to reproduce the observed $\delta^{11}B_{carb}$ (see SM Section 6 for further details of the model scenarios).

We illustrate the effect of uncertainties in $\delta^{11}B_{SW}$ and temperature on pH, and the overall consistency with the $\delta^{11}B_{carb}$ data in Figure S3 and Table S1 (note that the full model described in SM 4 also includes a dynamic calculation of temperature). The lowest $\delta^{11}B_{SW}$ =34‰ and highest pH considered (scenario CO_2*Lo*) is effectively constrained by the model limitation on the highest pH values immediately prior to EP1. The highest $\delta^{11}B_{SW}$ =36.8‰ and lowest pH (scenario CO_2*Hi*) is effectively constrained by the limit of propagated uncertainty (2σf) on the lowest observed $\delta^{11}B_{carb}$ combined with the non-linearity of the B isotope system.

An additional uncertainty in interpreting $\delta^{11}B_{carb}$ is introduced by any potential offset or fractionation between seawater borate $\delta^{11}B(OH)_4^-$ and $\delta^{11}B_{carb}$. The laboratory measured fractionation of abiotic carbonate (*66*) shows both an offset relative to that of the artificial seawater, and a shallower slope with increasing pH (*61*). As we consider $\delta^{11}B_{SW}$ as a model parameter to be determined, an overall offset is effectively subsumed within this. However a shallower slope than that used here ($^{11-10}K_B$ = 1.0272 (*61*) cf. the one given for inorganic carbonates (1.0267; (*66*)) would require a larger pH change for a given observed change in $\delta^{11}B_{carb.}$. To date, there is no agreement as to the actual deviation of inorganic calcite precipitates (*66)* from the now generally-accepted empirical fractionation factor (*61*) and a best fit value of 1.0267 for the inorganic calcite precipitation has been suggested (*67*). But by contrast, the deviation between the inorganic carbonate values and the empirical fractionation does appear to be much bigger and the best-fit value is given as 1.0260 (*61*). This increased deviation is explained by the difference in pH scale between natural or artificial seawater used for the calibration experiments, and the experimental seawater pH measured on the (freshwater) NBS scale. Boric acid incorporation may contribute to the ^{11}B enrichment observed in inorganic precipitates, especially at lower pH and hence may explain the deviation of $\delta^{11}B$ in inorganic precipitates from the empirical fractionation factor (*68*). However all carbonates precipitated under controlled pH conditions were enriched in ^{11}B relative to seawater borate (*68*).

If we use the best fit value of 1.0267 (*67*) for the inorganic carbonates (*66*) instead of the empirical value of 1.0272 (*61*) then the offset for the majority of the data would be around 0.05 pH units. Visible changes to more acidic values would only appear at the lowermost pH estimates, but would still be less than 0.2 pH units and fall within the general uncertainty. If we take the 1.0260 value, the offset would generally increase between ≤0.1 and 0.2 (pH range between ~8.4 and 7.8) but would indeed result in significantly lower pH values of up to 0.5 units for the acidification event.

Given the limited amount of experimental inorganic calcite data and this disagreement between the best-fit values, we have taken the simplest approach for the model representation and chosen to use the most generally-accepted empirical fraction factor (*68, 69*).

5. Model Description

5.1 Overview

The overall model structure (shown in Fig. S4) is essentially a superset of carbon cycle models previously applied to the end Permian (*14, 15, 70*), with additional consideration of the marine sulphur cycle. The model includes a three box ocean model as the minimum needed to demonstrate the effect of the biological pump on vertical DIC gradients and ocean redox state. The model is implemented as a set of coupled differential equations for the time evolution of reservoirs (Table S3), exchanging fluxes according to air-sea exchange, ocean circulation, applied external forcings and perturbations, and the biogeochemical processes described in Table S5. Model constants are defined in Table S4. The model implements an open inorganic carbon cycle, with atmospheric pCO_2 and marine DIC and Alk determined by the feedbacks between land-surface carbonate and silicate weathering and marine carbonate deposition. Oxidative weathering, volcanic degassing, and land and marine organic carbon burial are specified as forcings, as is marine phosphorus and hence productivity. The quantitative model uses previous estimates for background Early Permian conditions (*65, 71-73*) suggesting either high pCO_2 (CO_2*Hi:* ~10 PAL, pH ~7.5 $\delta^{11}B_{SW}$ ~36.8‰), or low pCO_2 (CO_2*Lo:* ~3 PAL, pH ~8, $\delta^{11}B_{SW}$ ~34‰).

5.2 Detailed description

5.2.1 pCO_2 and temperature

Global mean temperature T_{mean} is calculated from atmospheric pCO_2 using the energy balance model as in COPSE *(74, 75),* with solar insolation appropriate for 250 Mya. Marine temperature $T_{O(s,h,d)}$ is calculated from the global mean assuming a fixed high-low latitude temperature difference and minimum temperature of 2.5 ^{0}C, with $T_{O(s)}=T_{mean}+6.5$ ^{0}C and $T_{O(h,d)}=\max(T_{mean}-12.5,2.5)$ ^{0}C.

5.2.2 Land surface weathering, degassing, and organic carbon burial

Land surface weathering is essentially a stripped-down version of that in COPSE (*75*), with carbonate and silicate weathering included but sulphur weathering and the long-timescale sedimentary reservoirs for sulphur and carbon are omitted. Atmospheric oxygen is fixed at the present-day value. Silicate and carbonate weathering are controlled by atmospheric pCO_2 and temperature with functional forms:

$$f_{silw}=k_{silw}\, e^{0.090(T_{mean}-T_0)}[1+0.038(T_{mean}-T_0)]^{0.65}\left(\frac{2\,pCO_2}{1+pCO_2}\right) \quad \text{(S1)}$$

$$f_{carbw}=k_{14\_carbw}\,[1+0.087(T_{mean}-T_0)]\ \left(\frac{2\,pCO_2}{1+pCO_2}\right) \quad \text{(S2)}$$

where T_0=15 ^{0}C.

Atmospheric CO_2 is consumed, and carbon, alkalinity and calcium supplied to the ocean, according to the stoichiometry defined in Table S5. Volcanic degassing, oxidative weathering, and land organic carbon burial are prescribed as forcings.

5.2.3 Marine circulation and air-sea exchange

Marine circulation is defined by a thermohaline circulation T, and high-latitude – deep exchange f_{hd}. The marine box model includes P, O, DIC, Alk, SO_4, H_2S as per-box prognostic variables, along with DIC $\delta^{13}C$. Marine carbonate chemistry is calculated using a modified version of CO2SYS-MATLAB v1.1 (*62*), extended to include sulfide alkalinity using the

constants tabulated by (*76*). Air-sea exchange of oxygen and CO_2 assume a fixed piston velocity and temperature-dependent solubility.

5.2.4 Marine productivity and burial

Productivity and hence the biological pump are controlled by the marine phosphorus circulation. Biomass is produced in the surface ocean boxes, and exported and remineralized in the deep box according to the processes and stoichiometries defined in Table S5. Productivity in the 's' box is specified to consume all phosphorus down to negligible concentration. Productivity in the 'h' box is specified to consume a fraction 0.18 of input phosphorus. Remineralization in the deep ocean box consumes oxygen down to a limiting concentration of 1μM and thereafter reduces sulfate to sulfide.

Shallow-water carbonate deposition occurs in the 's' box only and is controlled by aragonite saturation state and a parameter representing a combination of shelf area and calcification effectiveness, ie a 'Neritic' ocean without pelagic calcifiers (*77*), functional form $k_{carbsedshallow}*(\Omega_{aragonite}-1)^{1.7}$. Ocean carbonate compensation is not included, on the basis this will be small for a 'Neritan' ocean.

Marine organic carbon burial from the 's' box and pyrite burial from the 'd' box are imposed as forcings. Given the uncertainties in controls on phosphorus input over the end-Permian interval, the marine phosphorus cycle is semi-closed (i.e. weathering feedback on phosphorus input is not included), with imposed perturbations (forcings) to source/sink balance (riverine input vs burial) applied as inputs to the 's' box to control phosphorus concentration.

5.2.5 Carbon isotopes

Carbon isotopes are implemented with additional reservoirs for each of atmospheric CO_2 and marine $DIC_{(s,h,d)}$. Air-sea exchange fractionates according to the temperature-dependent equilibrium and kinetic factors determined by Zhang et al. (*78*). Marine export production is at fixed fractionation relative to DIC, with $\delta^{13}C_{exp(s,h)}= \delta^{13}DIC_{(s,h)} - 25$ ‰.

Volcanic degassing, carbonate weathering, and oxidative weathering are assumed to add carbon at fixed fractionations of -4.9‰, 2.65‰, and -25‰ respectively. Atmospheric CO_2 consumed by silicate and carbonate weathering (and added to the ocean 's' box as DIC) is fractionated relative to atmospheric CO_2 according to the freshwater fractionation of Zhang et al. (*78*).

Land and marine organic carbon burial is at fixed fractionation relative to atmospheric CO_2 and marine DIC, with $\delta^{13}C_{locb}= \delta^{13}CO_2$-19 ‰ and $\delta^{13}C_{mocb}= \delta^{13}DIC_{(s)}$-25 ‰. Marine inorganic carbon burial is assumed to not fractionate relative to $DIC_{(s)}$.

5.2.6 Boron isotopes

Carbonate-associated boron isotopic composition $\delta^{11}B_{carb}$ is assumed to be equal to that of seawater $B(OH)_4^-$. Speciation of $B(OH)_4^-$ and $B(OH)_3$ is calculated using CO2SYS-MATLAB v1.1 *(62)*. Isotopic composition is then calculated from speciation $x_{bo4} = [B(OH)_4^-]/[B\ total]$ and seawater $\delta^{11}B_{SW}$ as

$$\delta^{11}B_{carb} = \frac{\delta^{11}B_{sw} - 1000(1 - x_{bo4})(\alpha_B - 1)}{\alpha_B - x_{bo4}(\alpha_B - 1)}$$

with the isotopic fractionation factor $\alpha_B = 1.0272$.

5.2.7 Model spinup and steady state

The model pCO_2 steady-state is defined by the imposed degassing rate, organic carbon burial and oxidation, and silicate weathering parameterisations, where these together define a

unique value for the steady-state atmospheric pCO_2 and temperature where $f_{ccdeg}+f_{oxidw} = f_{silw}+f_{locb}+f_{mocb}$. During spin-up, the ocean chemistry and hence atmosphere-ocean CO_2 partitioning adjust (on the silicate weathering timescale of ~100kyr) to a steady-state, with the aragonite saturation state adjusting such that carbonate burial balances inputs from carbonate and silicate weathering.

5.2.8 Sensitivity to seawater composition

The Mg and Ca composition of end-Permian seawater (as determined from fluid inclusions) is consistent with that of modern seawater ([Mg] = 53 mmol/kg, [Ca] = 10.3 mmol/kg), but with large uncertainties (*79*). Sulfate concentration may have been much lower than modern values (*80, 81*). We estimate the uncertainties in carbonate system chemistry following the approach of (*82*). We estimate the effect on K_1 and K_2 from model results (*83*) as:

$$\frac{K_1^*}{K_1} = 1 + 0.155\frac{\Delta[Mg^{2+}]}{[Mg^{2+}]_m} + 0.033\frac{\Delta[Ca^{2+}]}{[Ca^{2+}]_m} - 0.019\frac{\Delta[SO_4^{2-}]}{[SO_4^{2-}]_m}$$

$$\frac{K_2^*}{K_2} = 1 + 0.641\frac{\Delta[Mg^{2+}]}{[Mg^{2+}]_m} + 0.071\frac{\Delta[Ca^{2+}]}{[Ca^{2+}]_m} - 0.054\frac{\Delta[SO_4^{2-}]}{[SO_4^{2-}]_m}$$

where subscript m refers to modern values and an asterix to end-Permian values. Taking extremal values $[Mg^{2+}]^*/[Mg]_m=0.5$, $[Ca^{2+}]^*/[Ca]_m=2$, $[SO^{2-}{}_4]^*/[SO^{2-}{}_4]_m=0.1$, we have K_1^*/K_1=1-0.078+0.033+0.0171=0.972 or $pK_1^*=pK_1+0.012$ (or for $[Mg^{2+}]$ alone, K_1^*/K_1=0.92, $pK_1^*=pK_1+0.035$). For a fixed pCO_2, this implies a corresponding decrease in $[HCO_3^-]$ and hence DIC inventory, or equivalently an increase in pH for the same DIC content. The corresponding effect on K_2 is much larger, K_2^*/K_2=1-0.32+0.0171+0.049=0.75.We estimate the effect of Mg concentration on the calcite solubility constant K_{sp} using the parameterisation given by (*82*) as:

$$\frac{K_{sp}^*}{K_{sp,m}} = 1 - 0.0833\left(\frac{[Mg^{2+}]_m}{[Ca^{2+}]_m} - \frac{[Mg^{2+}]^*}{[Ca^{2+}]^*}\right)$$

which gives K_{sp}^*/K_{sp}=1-0.33.

This sensitivity study shows that the uncertainty in K_1 therefore introduces only a small uncertainty in pH (~< 0.03) or equivalently a ~10% uncertainty in DIC inventory relative to pCO_2. The combined uncertainties in K_2, K_{sp} and $[Ca^{2+}]$ are larger, introducing corresponding uncertainties in calcite saturation state. However, within the model employed here, this is effectively absorbed into a rescaling of the parameter $k_{carbsedshallow}$.

6- Model Scenarios

Given the uncertainty in the absolute value of the seawater boron isotope composition (section S4), we consider two scenarios with initial steady-state conditions as in Table S6: scenario CO_2*Hi* uses $\delta^{11}B_{SW}$=36.86, and CO_2*Lo* uses $\delta^{11}B_{SW}$=34. Here ocean pH depends on the combination of atmospheric pCO_2 and carbonate saturation state. Atmospheric pCO_2 (set by the ratio of net carbon sources : silicate weatherability) is tuned to 3 or 10 PAL, encompassing the range of conditions considered by previous model studies *(73, 84)*. Ocean carbonate saturation state is set by carbonate sedimentation efficiency parameter $k_{carbsedshallow}$, which represents a combination of shelf area x deposition rate. A summary of scenarios required to explain the three events in our $\delta^{11}B$ data are given in Table S7 and explored in further detail below.

6.1 Mechanisms for pH rise

The rise in $\delta^{11}B$ at 252.05 Ma corresponds to a rise in pH from 7.5 to 8.0 for scenario CO_2*Hi*, and from 8.0 to 8.3 for scenario CO_2*Lo.* Given the major upheavals in the Earth system at the end-Permian, multiple mechanisms including changes in silicate and carbonate weathering, and marine changes in calcification and due to anoxia may potentially contribute to pH rise, and we use model sensitivity studies to determine potential constraints. We first review evidence for each mechanism, then summarize the model sensitivity studies and propose plausible scenarios involving multiple drivers.

6.1.1 Carbonate weathering

The overall high weathering rates across the Permian-Triassic boundary also imply an increase in carbonate weathering, possibly combined with any direct effect from chemical weathering of eroded clastic material itself.

There is also direct evidence for later sea-level regression and subaerial weathering of the shallowest sections of the S. China carbonate platform, coincident with EP1 *(23)* which may contribute to maintaining pH over this interval. To estimate an order of magnitude for enhanced carbonate shelf weathering: 10^{18} mol $CaCO_3$, density 2.8 g cm^{-3} has volume 36,000 km^3, or 100m x $3.6x10^5 km^2$, or 1800km of 200km wide shelf; this would provide a weathering flux of 10^{13} mol $CaCO_3$ yr^{-1} for 100 kyr, comparable to the background carbonate weathering rate.

6.1.2 Decrease in calcification effectiveness

Overall global biotic calcification effectiveness is determined by the combination of available shelf area, and local ecosystem-dependent rates. A reduction in area of deposition could be because anoxic/euxinic waters extend onto the shelf bottom precluding those parts from hosting deposition, and/or because there is a sea level change reducing shelf area. The input of clastics prior to EP1 could also reduce carbonate production as a result of ecosystem impacts (*85, 86*).

6.1.3 Productivity-driven ocean anoxia, sulfate reduction, and pyrite burial

Multiple lines of evidence suggest a (large) expansion of oxygen minimum zones prior to the PT boundary, while the deep ocean remains suboxic. These include U isotope evidence for ~6x increase in anoxic fraction (*87*), extensive pyrite deposition (*88*), and GCM studies (*89*) illustrating the spatial distribution of anoxia.

We represent productivity-driven ocean anoxia by increasing marine phosphorus from the present-day value to 2.3x present (the value used by (*66*). This is achieved by adding phosphorus to the marine 's' reservoir (representing a net excess of riverine input over sediment output) at rate $3.9x10^{10}$ mol yr^{-1} over the interval 252.15 – 252.05 Ma (cf present-day riverine input $\approx 2x10^{10}$ mol yr^{-1}) (*75*). This results in pCO_2 drawdown as a result of the increased biological pump, and in sulfate reduction leading to ~ 50 μM H_2S in the 'd' box. Note that sulfate reduction increases alkalinity / pH in the 'd' box by ΔpH ~ 0.1, but as the S redox shuttle is completed by sulfide oxidation at the base of the oxic surface box, this has no effect on the pH of the oxic surface ocean.

High rates of pyrite formation are seen at and before EP1 (*88, 90*). Pyrite burial results in a net alkalinity source (*91*). We assume that pyrite deposition is a water-column process, hence is limited by the availability of iron and sulfide. The most limiting factor for the scenarios considered here is iron. To quantify this, we estimate pyrite deposition rate sustainable over a timescale of ~100kyr as $\sim 1.25x10^{12}$ mol FeS_2 yr^{-1}, based on availability of reactive iron Fe_{HR} (in the contemporary oxic ocean, Fe_{HR} total input to the ocean is ~ $6.8x10^{12}$ mol yr^{-1}, of which only $\sim 1.3x10^{12}$ mol yr^{-1} gets to the deep ocean (*87*). Sulfide availability is determined by anaerobic organic carbon remineralisation in the 'd' box, which is a model-

determined fraction of total export production ~10^{14} mol yr^{-1}, and is less limiting than iron for the scenarios considered here. This assumes that sulfate for remineralisation (and hence sulfide availability) is unconstrained by marine sulphur availability, ie that the marine sulfate reservoir is drawn down. This is supported by (or at least consistent with) the data indicating low early Triassic marine sulfate, < 4mM (*80, 81*).

6.1.4 Silicate weathering

Anomalously high sediment fluxes across the Permian-Triassic boundary (*85, 86*) imply soil loss and increased exposure of highly weatherable rock surfaces, with increases in both physical and chemical weathering. Early Siberian traps emplacement and an increase in area of weatherable basalt also may contribute to an increase in overall silicate weatherability. The main increase in silicate weathering is seen in the Griesbachian but increases may have acc ompanied the carbon injection for EP1.

6.1.5 Combined scenarios

We summarize the effect of illustrative perturbations for the separate contribution of each potential driver of pH increase in Table S8. Perturbations were applied to the CO_2*Lo* steady state at 251.95Ma (corresponding to the pH rise seen in the $\delta^{11}B$ data), with effect shown 100kyr later (at EP1). The marine carbonate system responds on a timescale of ~10kyr, hence reaches a steady state source-sink balance, however the timescale for land-surface weathering feedbacks is >~100 kyr hence the system does not reach a steady state. The dynamic response is included in the full scenarios.

As shown in Fig. S5, the perturbations fall into two groups. Increases in silicate weatherability and pyrite deposition leave carbonate input rate and calcification output essentially unchanged, hence result in changes to atmospheric pCO_2 at nearly constant saturation state. Changes to atmospheric pCO_2 alone are unable to produce a change in pH or $\delta^{11}B$ as large as that seen in the data without implausibly low pCO_2 and hence temperature, hence these cannot be the sole drivers of pH increase. Reductions in calcification effectiveness or increases in carbonate inputs change both the carbonate system saturation state and atmospheric pCO_2, resulting in a much larger increase in pH for a given decrease in pCO_2. A major contribution from either or both of these mechanisms is therefore required.

The results from the perturbations study demonstrate that all mechanisms may contribute to pH rise, with a major contribution from either or both carbonate input and decrease in calcification effectiveness required. Given the most likely case where multiple mechanisms all contribute, we construct scenarios with a decrease in calcification effectiveness as the major component and smaller contributions from pyrite burial and carbonate weathering (Fig. S6). The perturbations considered for the two scenarios are summarized in Table S9 and the dynamic response is shown in Fig. S6.

6.2 Sources of carbon and volatiles causing a negative $\delta^{13}C$ excursion or pH excursion

6.2.1 Terrestrial Carbon burial

The effect of destruction of the land biota and a corresponding decline in land organic carbon burial at the PT boundary was first considered by Broecker and Peacock (*16*). We represent this by setting land organic carbon burial to zero at T=251.95Ma, resulting in a drop in $\delta^{13}C_{carb}$ of ≈ 4‰ (comparable to that seen in end-Permian sections), but over timescale of ~100kyr.

6.2.2 Marine Carbon burial

Despite (or because of) ecological shifts to a cyanobacteria dominated ecosystem (*92*), proxy evidence for continued high sediment organic carbon fluxes (*90*) and a vertical $\delta^{13}C$ gradient (*93, 94*) as well as continuing marine anoxia suggests that high marine productivity continues through Permian-Triassic. Interruption to the marine biological pump would result in a short timescale (ocean circulation timescale ~10^3 yr) increase in surface ocean pH and decrease in surface ocean (and hence carbonate) $\delta^{13}C$. This was considered as a mechanism for short-timescale $\delta^{13}C$ fluctuations over the PT interval (*15*). We do not consider this further here as this mechanism results in coupled perturbations to both surface ocean pH and $\delta^{13}C$, and hence cannot be the major driver for the '$\delta^{13}C$ without pH' or 'pH without $\delta^{13}C$' signals. Smaller perturbations (interruptions) to the biological pump may be plausible as a contributor to short-timescale $\delta^{13}C$ signals following EP1.

6.2.3 Siberian traps volcanism and contact metamorphism

In order to bound plausible model scenarios, we review here potential mechanisms for volatile input from the Siberian Traps and summarise constraints on magnitudes and rates, based on (*26, 33, 95*).

The Siberian Traps magma area is estimated as 2.5 – 5x10^6 km^2 and volume > 2x10^6 km^3. This intruded into the Tungska sedimentary sequence, which reaches 12.5 km in thickness and includes. ≈2.5 km of Cambrian evaporites containing abundant limestone, halite, dolomite and anhydrite (*26, 33*), coal deposits, as well as Neo-Proterozoic petroleum-bearing shale and carbonate. Intrusion of magma into the sediments resulted in abundant sills and dykes with accompanying contact aureoles, and explosively-generated pipes. The igneous province is estimated to contain approximately 50% intrusive dykes and sills, 30% basalt lava flows, and 20% pyroclastic material (*96, 97*).

The volume of sediments affected by contact metamorphism is estimated (*26*) from a sill area of 2x10^6 km^2, thickness 200m, generating a contact aureole of thickness 400m. This results in potential release of 0.8-2.3x10^{18} mol C (as isotopically light methane and CO_2) from metamorphic degassing of organic carbon (assuming the TOC weight percent reacted is 0.5 – 1.5%), over a timescale ≈50kyr. In addition, pipes (each with source region ≈5 km^3) could release 0.1 – 0.3x10^{18} mol C over ≈6.5 kyr. Intrusion into carbonates could release comparable quantities of isotopically-heavy CO_2 via calcsilicate formation and decarbonation of dolomite into periclase and calcite, and intrusion into

anhydrite could release comparable quantities of S as SO_2 (*98*). Interaction between petroleum-bearing inclusions and host rock salt could in addition generate halocarbons, estimated at 1-3x10^{17} mol CH_3Cl (*26*). Intrusion into coal-seams could result in explosive interaction resulting in large-scale coal combustion (*95*).

The Siberian Traps magmas contain anomalously high quantities of S, Cl, F *(33),* estimated to result in total intrusive and extrusive degassing of 0.2-0.25x10^{18} mol S, 0.1-0.25 x10^{18} mol Cl, and 0.4-0.7 x10^{18} mol F *(33)*. The ultimate source of these volatiles is likely to be assimilation from sedimentary host rocks.

6.2.4 Carbon injection perturbations

Given the episodic nature and likely variability in isotopic composition of carbon additions from Siberian Traps volcanism and contact metamorphism, we consider size, rate, and isotopic composition of carbon additions via sensitivity studies within plausible ranges.

The effect on $\delta^{13}C_{carb}$ of a carbon addition of isotopic composition $\delta^{13}C_{carb}$ is given approximately by mass-balance with the surface (atmosphere and ocean) carbon reservoirs *(73, 84).* The effect on pH is additionally dependent on the rate of addition. We show in Table S10 model results for combinations of addition size, isotopic composition and rate, constrained to result in $\delta^{13}C_{carb}$ = -3 ‰, demonstrating the additional non-linear effect of land-surface weathering feedbacks ('land carbonate compensation').

The decline in $\delta^{13}C_{carb}$ over the P-T boundary is faster than can be accounted for by a decrease in land carbon burial alone, implying an additional pulse of isotopically light carbon contribution ~-2‰ to the decline. We show in Figure S7 the constraints from the $\delta^{11}B$ data on carbon additions over the 50kyr interval 251.95 – 251.90 Ma. The results demonstrate that providing the rate of carbon addition is relatively slow as here, the pH constraints are in fact relatively weak, and are consistent with a range of input isotopic compositions $\delta^{13}C_{inj}$.

The acidification event at ~251.89Ma requires a rapid addition of carbon on a timescale ≤ 10 kyr, with an isotopic composition $\delta^{13}C_{inj}$≈0 ‰ in order to leave $\delta^{13}C_{carb}$ unaffected, and size ≥ 2x10^{18} mol in order to produce a sufficient decline in pH and $\delta^{11}B$ (Figure S8). Larger (or more rapid) carbon additions produce relatively little additional response in ocean pH, as the majority of the input carbon remains in the atmosphere, and the response of the $\delta^{11}B$ is also non-linear at low pH. The rate of the inferred carbon addition is ~3 times the estimates above for organic carbon from the combined effects of sills (0.16 – 0.4 x10^{18} mol C over 10 kyr) and pipes (0.1 – 0.3 x10^{18} mol C over ~6.5 kyr), but is not unreasonable given the carbonate carbon source and large uncertainties in these estimates.

6.2.5 SO_2 injection perturbation

Contact metamorphism of evaporites resulting in large SO_2 release could potentially also contribute to the acidification event. Quantitatively the effect (per mol) on ocean pH is approximately twice that of a carbon addition, and given the relative abundance of

evaporites to carbonates is therefore likely to represent a smaller contribution to acidification.

Fig. S1

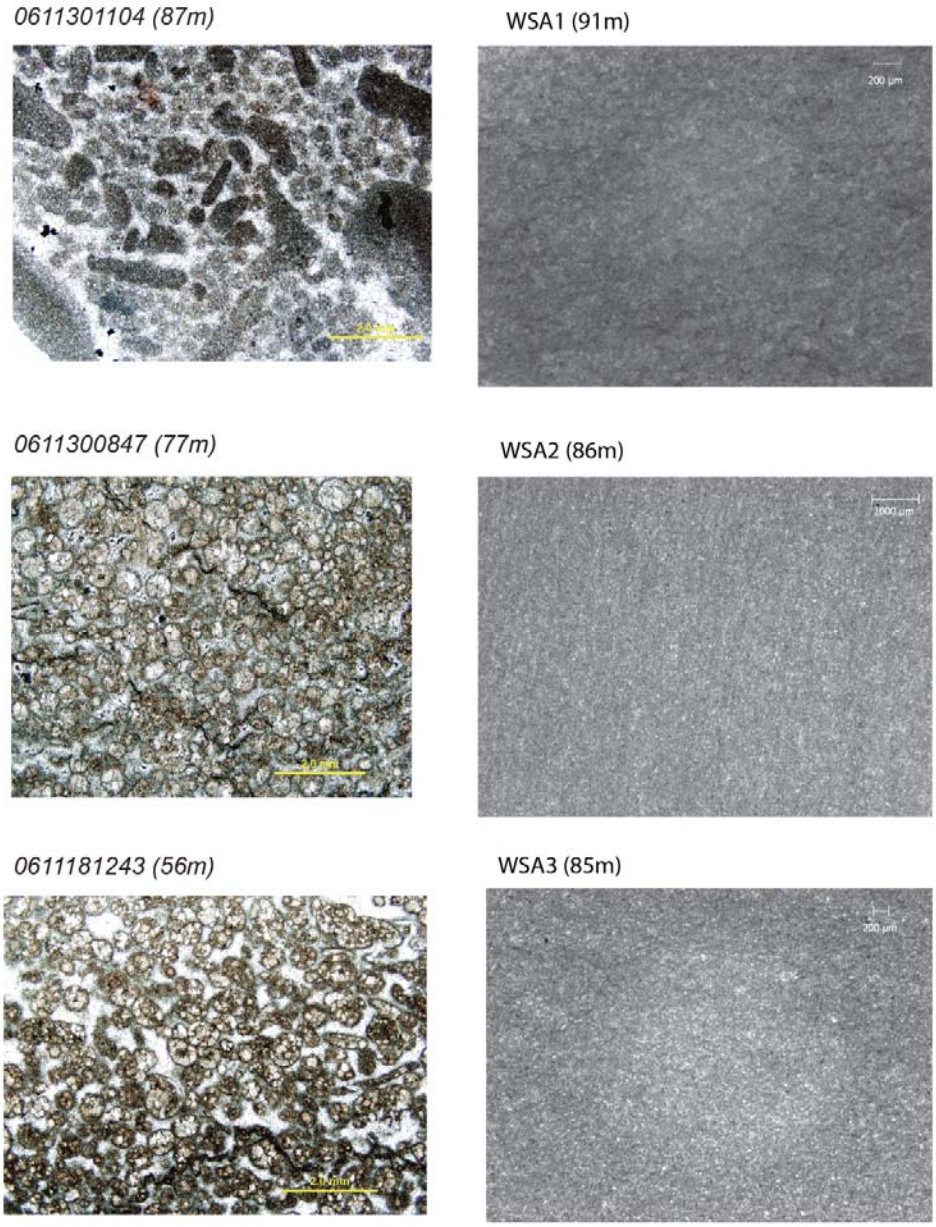

Examples of thin section images for the Wadi Bih section, WSA transect. WSA samples demonstrate homogeneous micritic texture of samples used for $\delta^{11}B$ analysis. 06- samples are previously published (38) illustrating grainstones. The lack of compaction of grains

and pore filling equant spar cements indicate very early/syn-sedimentary cementation. This fabric is consistent with indicators for supersaturated conditions in this interval, including thrombolites and flat pebble conglomerates, and suggests preservation of the original depositional fabric. Sample heights (m) given as in Fig. 1 and Table S1.

Fig. S2

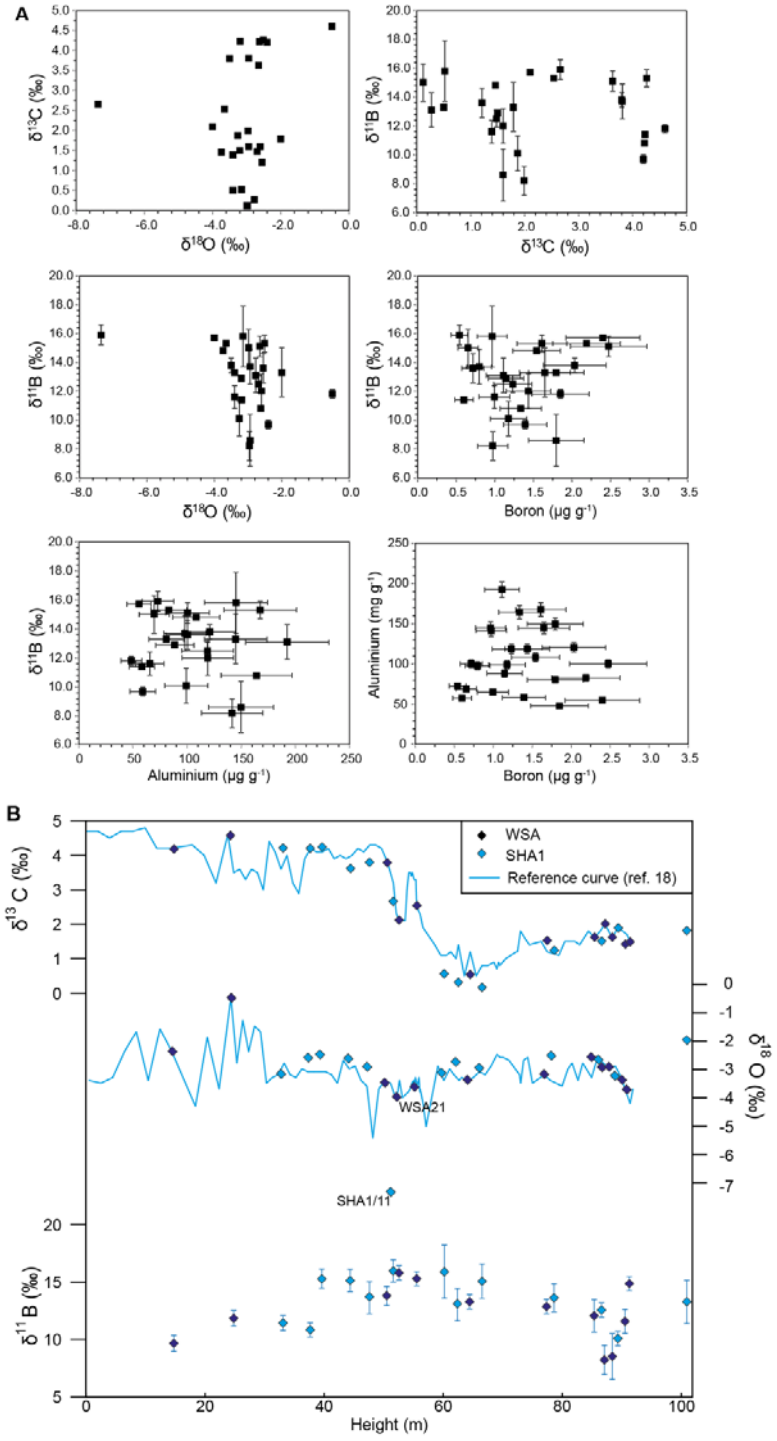
A
δ13C (‰)
δ18O (‰)
δ11B (‰)
δ13C (‰)
δ11B (‰)
δ18O (‰)
δ11B (‰)
Boron (µg g-1)
δ11B (‰)
Aluminium (µg g-1)
Aluminium (mg g-1)
Boron (µg g-1)
B
WSA
SHA1
Reference curve (ref. 18)
δ13 C (‰)
δ18 O (‰)
WSA21
SHA1/11
δ11 B (‰)
Height (m)

Isotope and elemental plots for the Wadi Bih sections. **A** Cross-plots of boron, carbon, and oxygen isotope data (2σ) and boron and aluminium concentration (2σr) for the marine carbonate samples from Wadi Bih. No significant correlation can be observed. **B** Shallow water $\delta^{13}C$ and $\delta^{18}O$ record from (*18*) and $\delta^{11}B$ (2σf uncertainty) record plotted against height (m). Symbols denote data from this study where WSA are replicate analysis of the same samples as the reference curve. SHA1 samples are from the second transect. Only SHA1/11 shows a more negative $\delta^{18}O$ value, but despite this they replicate within uncertainty for $\delta^{11}B$ and the trends are not affected if this sample were rejected.

Fig. S3

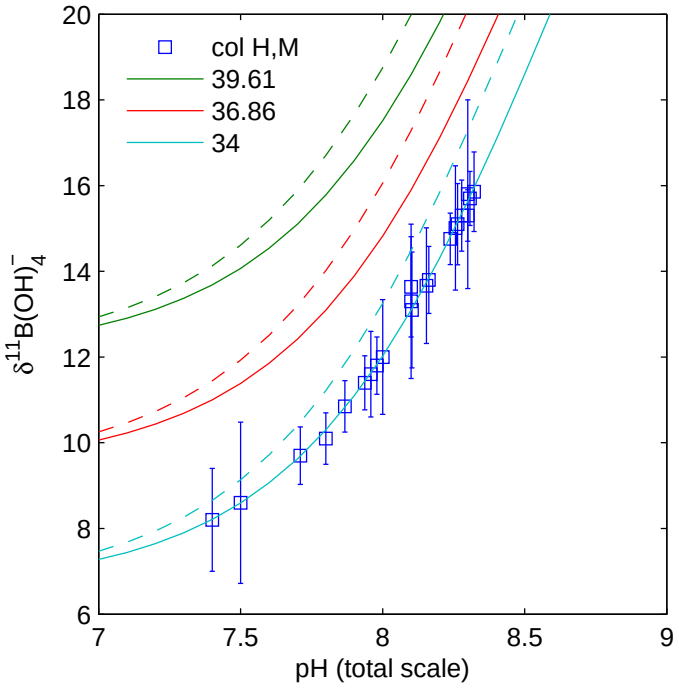

Effect of background $\delta^{11}B_{SW}$ and temperature on relationship between $\delta^{11}B_{carb}$ and pH (total scale), for conditions appropriate to low-latitude surface ocean (atmospheric pressure, salinity 35 psu, temperature 25˚C (solid lines) and 35˚C (dashed lines)). Three values are shown for $\delta^{11}B_{SW}$: 39.61‰ (the contemporary value) and two values consistent with the end Permian data. Data points and 2σf errors are overlaid for the $\delta^{11}B_{SW}$ 34‰ case.

Fig. S4

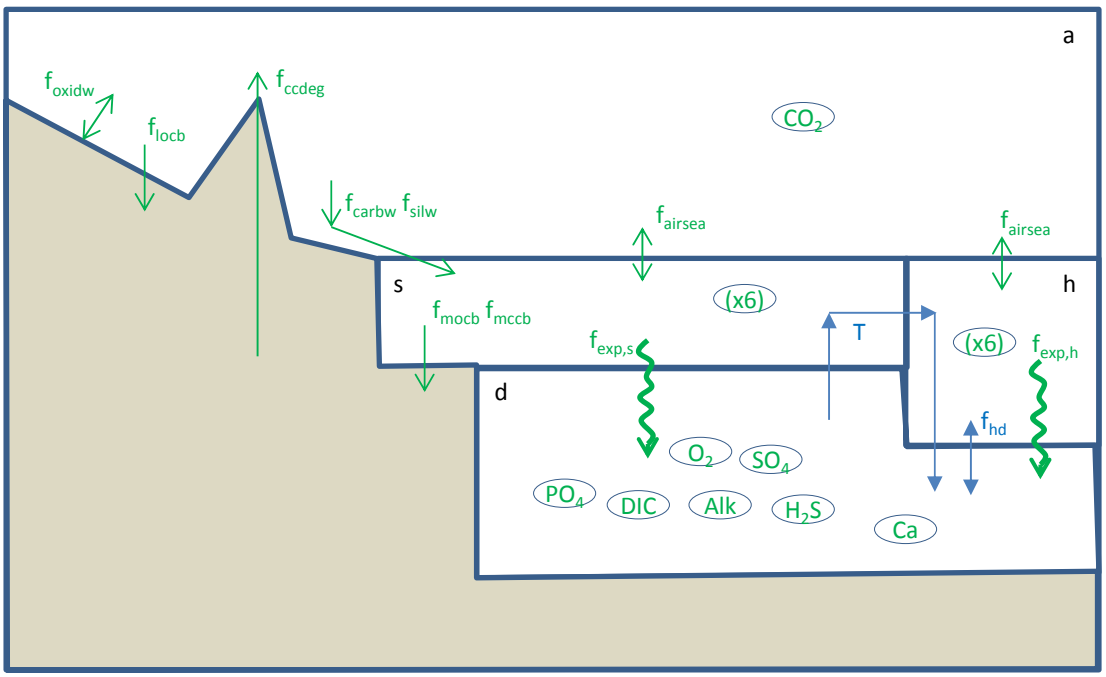

Model schematic. Ocean is represented by three boxes (s, h, d), with well-mixed atmosphere box a. Biogeochemical fluxes are shown in green, ocean circulation in blue. Biogeochemical reservoirs are shown as ovals.

Fig. S5.

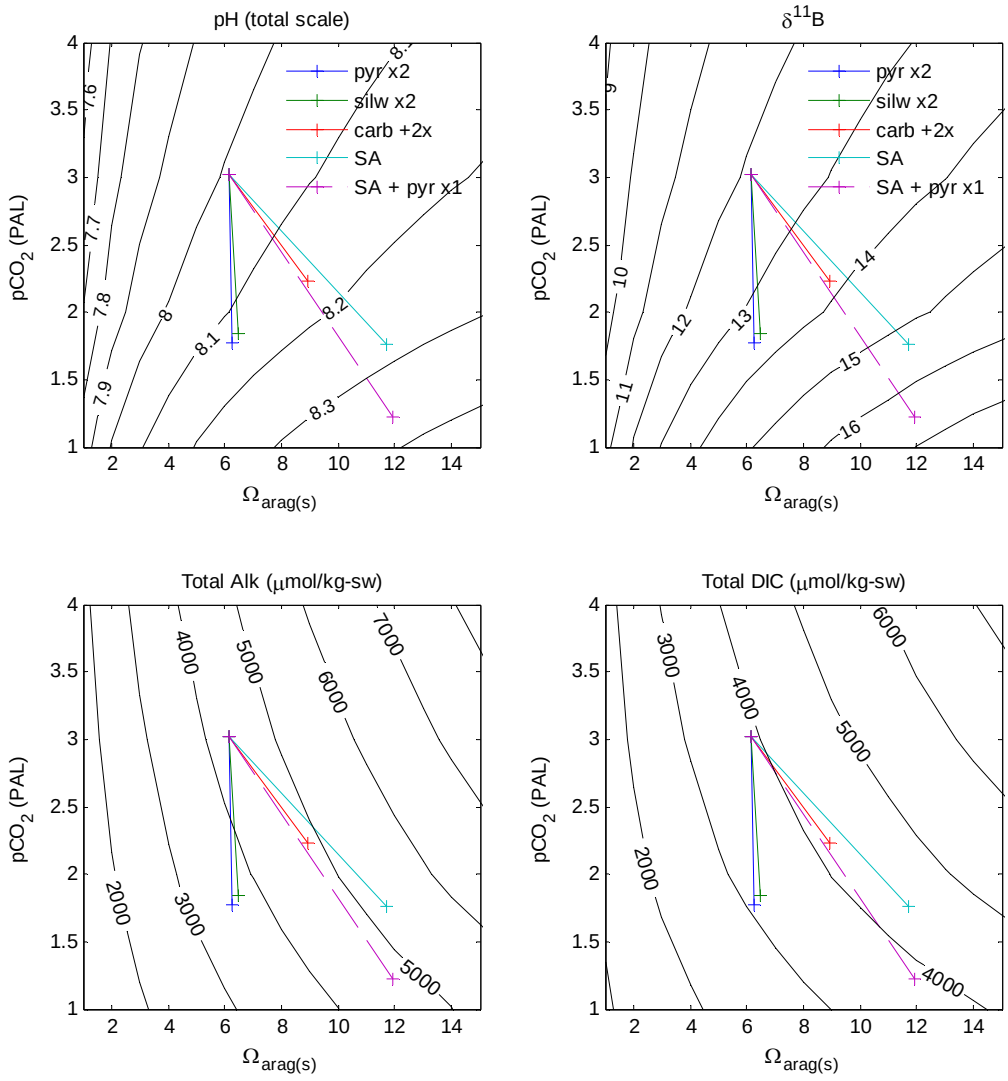

Effect of illustrative perturbations (defined in Table S8) on carbonate system properties for atmosphere and ocean surface (s) box. Contours show carbonate system parameters

for a constant temperature of 25 °C, salinity 35 psu, pressure 1 atm, hence do not exactly correspond to the full model results with varying temperature.

Fig. S6.

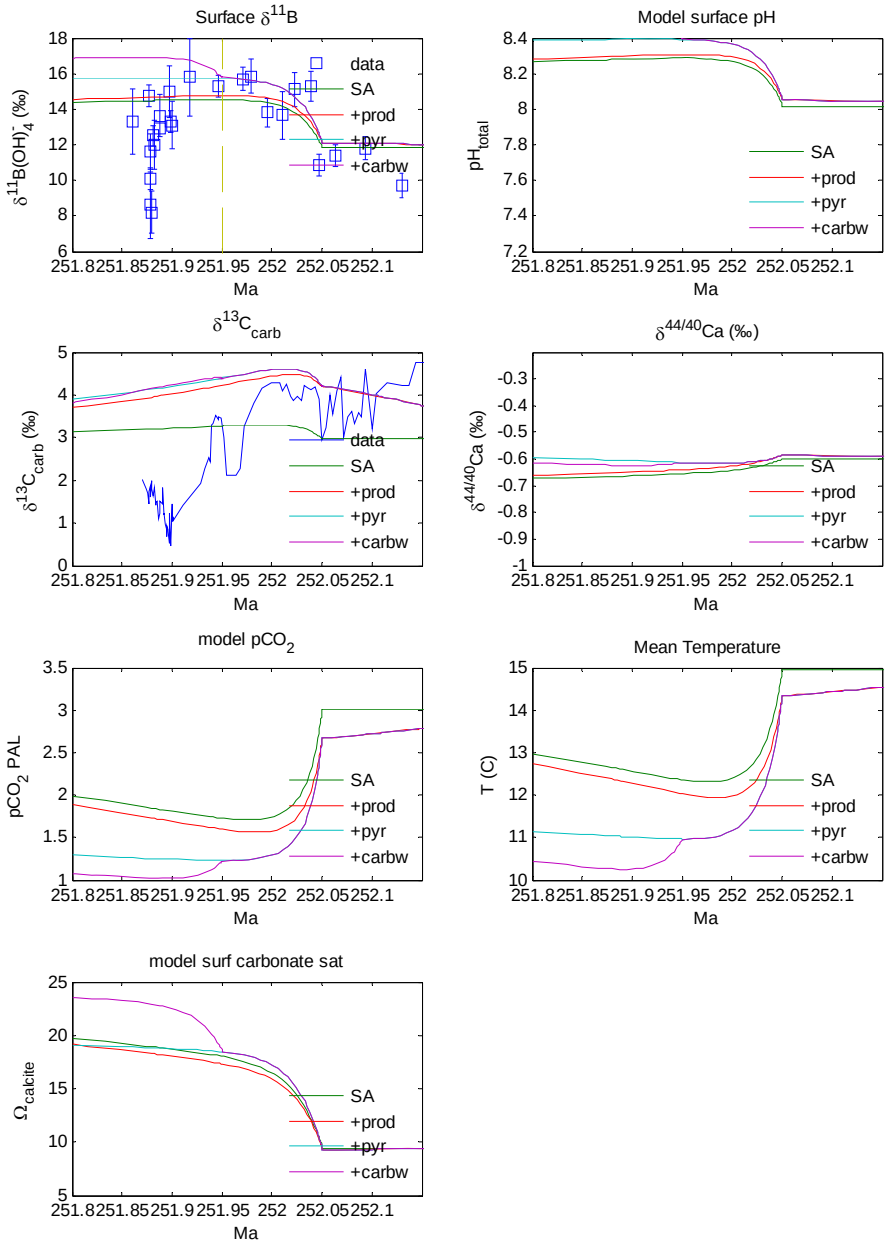
Surface δ11B
δ11B(OH)4- (‰)
data
SA
+prod
+pyr
+carbw
Ma
Model surface pH
pHtotal
δ13Ccarb
δ13Ccarb (‰)
δ44/40Ca (‰)
δ44/40Ca (‰)
model pCO2
pCO2 PAL
Mean Temperature
T (C)
model surf carbonate sat
Ωcalcite

Scenario CO_2*Lo*: Contributions to pH increase. ‘SA’: effect of calcification effectiveness decrease. ‘+prod’ effect of increased marine productivity and anoxia. ‘+pyr’ pyrite burial, and ‘+carb’ carbonate weathering.

Fig. S7

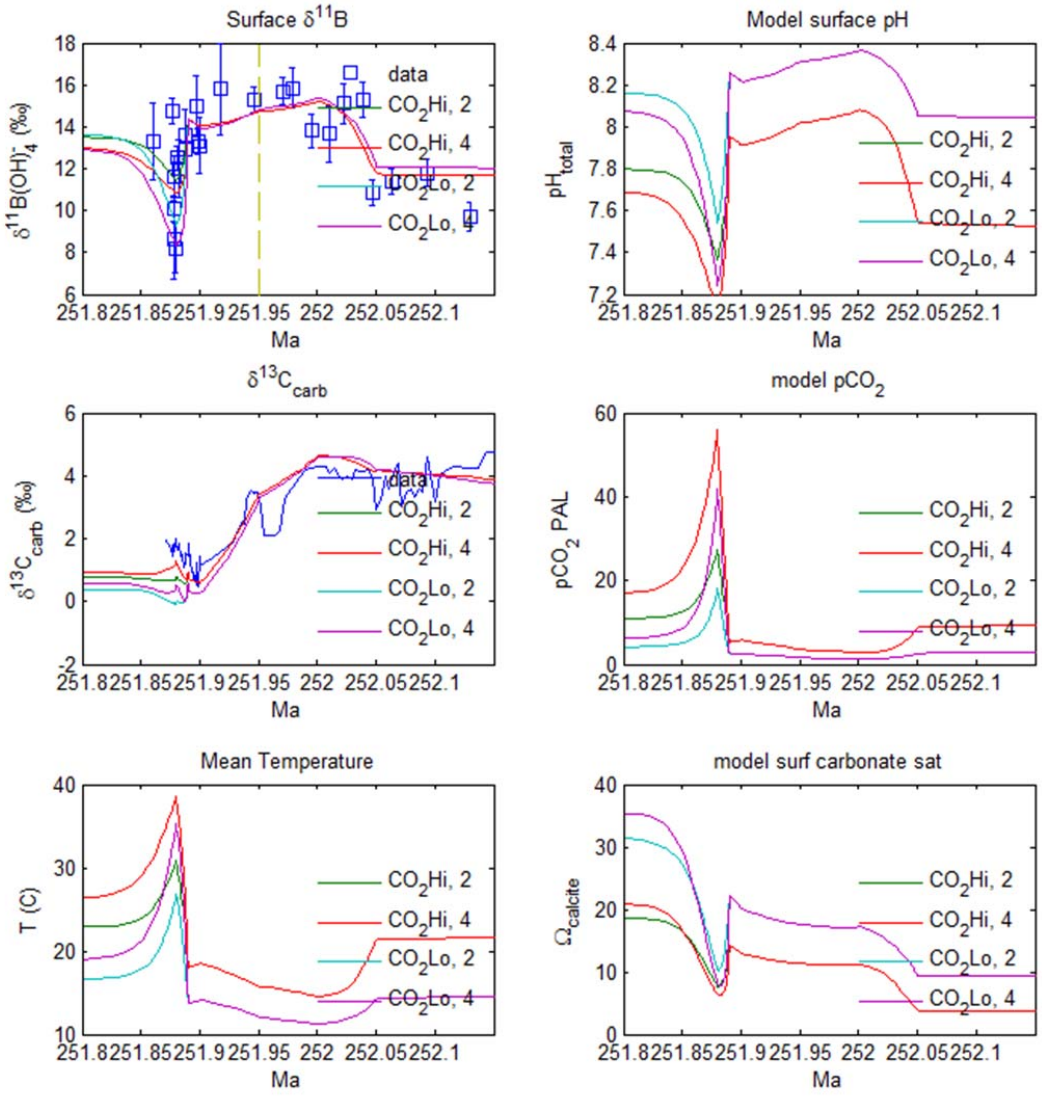

Effect of changing size of CO_2 input perturbations applied to scenarios *CO_2Hi* and *CO_2Lo* over 10kyr interval 251.89 – 251.88 Ma. Perturbation sizes are $2x10^{18}$ mol and $4x10^{18}$ mol. Isotopic composition is 2.65 ‰, i.e. equal to that of sedimentary carbonate.

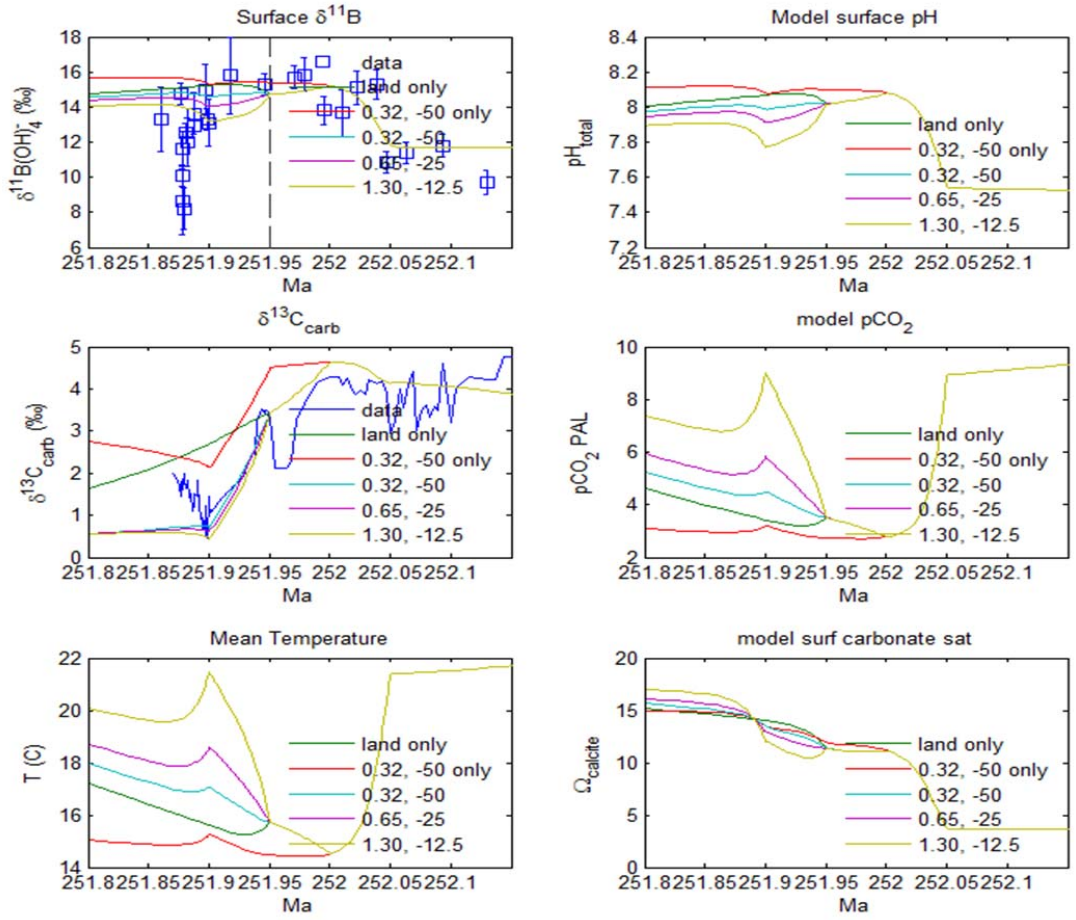

Fig. S8

Effect of changing size and isotopic composition of CO_2 input perturbations applied to scenario *CO_2Hi* over 50kyr interval 251.95 – 251.90 Ma. 'land only' shows the effect of interruption in land organic burial,'0.32. -50 only' shows the effect of carbon addition only. Other lines show combined effect of land burial and carbon addition. Perturbations are constructed to result in $\delta^{13}C_{carb} \approx$ -2 ‰, and correspond to inputs of: 0.32×10^{18} mol / -50 ‰; 0.65×10^{18} mol / -25 ‰; 1.30×10^{18} mol / -12.5 ‰

Fig. S9

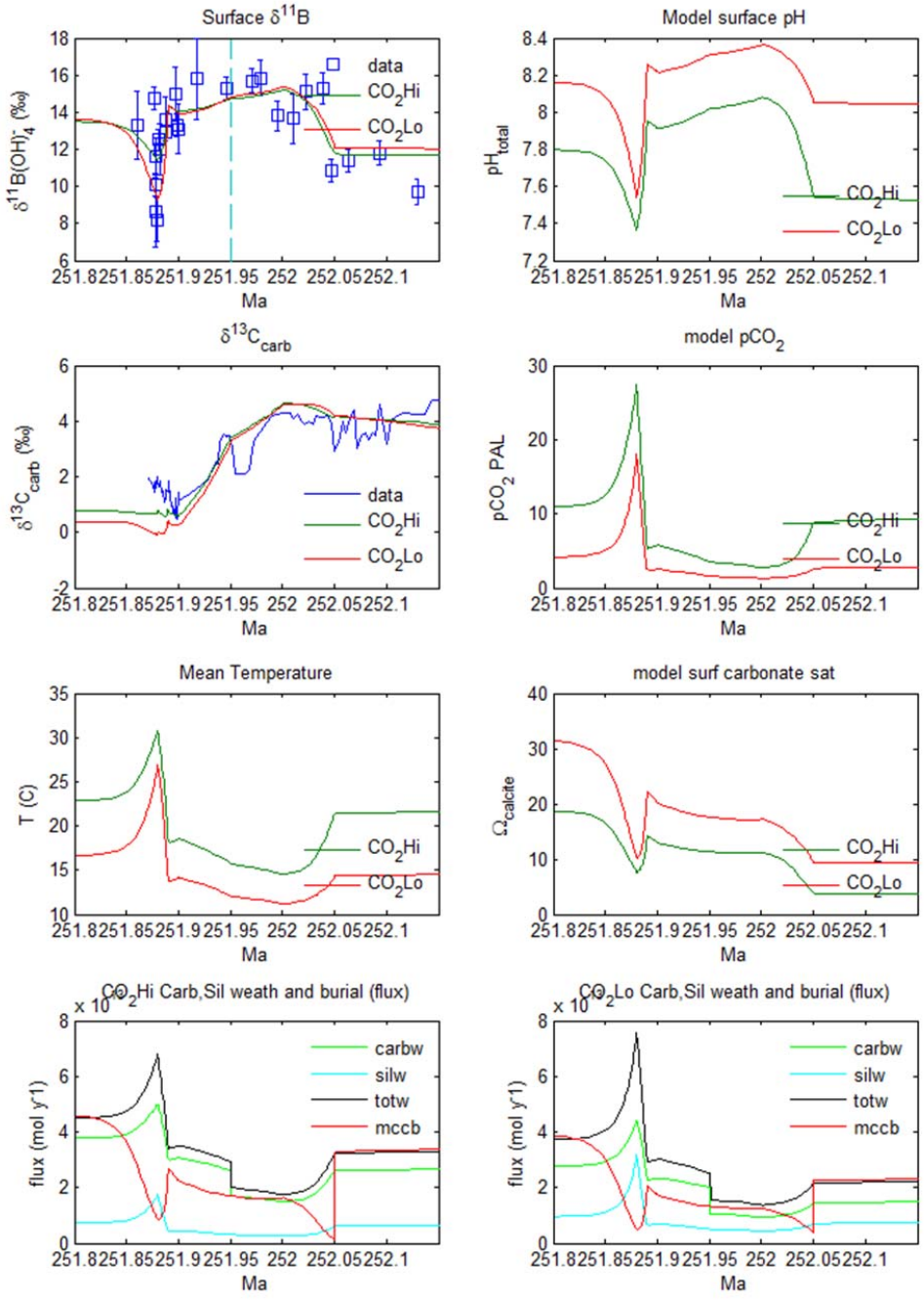
Surface δ11B
δ11B(OH)4- (‰)
data
CO2Hi
CO2Lo
Ma
Model surface pH
pHtotal
δ13Ccarb
δ13Ccarb (‰)
model pCO2
pCO2 PAL
Mean Temperature
T (C)
model surf carbonate sat
Ωcalcite
CO2Hi Carb,Sil weath and burial (flux)
CO2Lo Carb,Sil weath and burial (flux)
x 10^12
flux (mol yr1)
carbw
silw
totw
mccb

Additional model output for CO_2 scenarios shown in main paper Fig. 2. Weathering fluxes are shown for scenario *CO_2Lo* only. The different initial conditions (*CO_2Hi*, *CO_2Lo*) are detailed in Table S6. The overall scenario is outlined in Table S7, with the mechanisms for early pH rise discussed in section 6.1 and the carbon injections as detailed in the main text, and discussed in section 6.2.

Table S1.

Boron, carbon and oxygen isotope data from Wadi Bih (U.A.E); pH values are derived from a simplified and non-dynamic calculation using the $\delta^{11}B_{SW}$ range given by the model calculation and a constant pK_B for 25°C, 35 psu, 0 dbar.

Sample	Height (m)	Lithology	Age (Ma)*	$\delta^{13}C$ (‰)	$\delta^{18}O$ (‰)	$\delta^{11}B$ (‰)†	2σf (‰)‡	pH $\delta^{11}B_{SW}$ 34‰	pH $\delta^{11}B_{SW}$ 36.8‰
Wadi Bih (25° 50' 31.2"N 56° 06' 41.7"E)									
WSA54	14.0	micritic mudstone	252.13	4.20	-2.40	9.7(3)	0.7	7.7	6.7
WSA49	24.0	micritic mudstone	252.09	4.60	-0.50	11.8(3)	0.7	8.0	7.6
SHA1/1	32.4	dolograinstone	252.06	4.23	-3.19	11.4(2)	0.6	7.9	7.5
SHA1/3	37.0	grainstone	252.05	4.22	-2.62	10.8(0)	0.6	7.9	7.4
SHA1/4	39.0	micritic mudstone	252.04	4.26	-2.51	15.3(6)	0.8	8.3	8.1
SHA1/7	43.8	bioclastic packstone	252.02	3.63	-2.65	15.1(7)	1.0	8.3	8.0
SHA1/8	47.0	bioclastic packstone	252.01	3.81	-2.94	13.7(12)	1.4	8.2	7.9
WSA22a	50.0	micritic mudstone	252.00	3.80	-3.50	13.8(5)	0.8	8.2	7.9
SHA1/11	51.0	bioturbated mudstone	251.98	2.66	-7.36	15.9(7)	0.9	8.3	8.1
WSA21	52.0	micritic mudstone	251.97	2.10	-4.00	15.7(2)	0.6	8.3	8.1
WSA17	55.0	micritic mudstone	251.95	2.54	-3.65	15.3(2)	0.6	8.3	8.1
SHA1/15	59.6	calcisphere grainstone	251.92	0.52	-3.15	15.8(21)	2.2	8.3	8.1
SHA1/17	62.0	calcisphere grainstone	251.90	0.27	-2.77	13.1(12)	1.4	8.1	7.8
WSA12A	64.0	micritic mudstone	251.90	0.50	-3.40	13.3(0)	0.6	8.1	7.8
SHA1/20	66.0	calcisphere grainstone	251.90	0.12	-2.98	15.0(13)	1.5	8.3	8.0
WSA5A	77.0	micritic mudstone	251.89	1.50	-3.20	12.9(0)	0.6	8.1	7.8
SHA1/26	78.2	calcisphere grainstone	251.89	1.21	-2.55	13.6(10)	1.2	8.2	7.9
WSA3	85.0	micritic mudstone	251.88	1.60	-2.60	12.0(12)	1.3	8.0	7.6
SHA1/30	86.2	calcisphere grainstone	251.88	1.48	-2.69	12.5(6)	0.6	8.1	7.7
WSA2A	86.8	micritic mudstone	251.88	1.99	-2.96	8.2(10)	1.2	7.4	-

WSA2	88.0	micritic mudstone	251.88	1.60	-2.94	8.6(18)	1.9	7.5	< 7,0
WSA1B	89.0	micritic mudstone	251.88	1.87	-3.26	10.1(2)	0.6	7.8	7.0
SHA1/32	90.2	calcisphere grainstone	251.88	1.39	-3.40	11.6(8)	1.0	8.0	7.6
WSA1	91.0	micritic mudstone	251.88	1.46	-3.74	14.8(0)	0.6	8.2	8.0
SHA1/36	102.0	bioclastic packstone	251.86	1.79	-2.00	13.3(17)	1.8	8.1	7.8

* Ages are calculated based on tie points from Burgess et al. (2), see section S1.2

† External uncertainties for B isotope data are valid for the last digits (2σ)

‡ Propagated uncertainties for B isotope data

Table S2.

Elemental data from Wadi Bih samples on which δ11B was determined.

Sample	B μg g^{-1}	Mn μg g^{-1}	Sr μg g^{-1}	Ba μg g^{-1}	Fe μg g^{-1}	P μg g^{-1}	S μg g^{-1}	Al μg g^{-1}	Si μg g^{-1}	Mn/Sr	Mg/Ca (mol/mol)
WSA54	1.4	22	48	1.6	205	7	219	59	78	0.4	0.90
WSA49	1.9	18	56	0.7	217	6	115	48	40	0.3	0.89
SHA1/1	0.6	38	57	3.9	310	9	163	58	31	0.7	0.91
SHA1/3	1.3	33	55	4.4	249	17	52	164	155	0.6	0.90
SHA1/4	1.6	26	54	3.5	213	21	78	167	146	0.5	0.91
SHA1/7	2.5	29	84	2.1	101	25	128	100	98	0.3	0.91
SHA1/8	0.8	40	56	3.4	170	14	141	98	55	0.7	0.91
WSA22a	2.0	25	50	2.3	122	24	56	121	175	0.5	0.89
SHA1/11	0.5	96	86	8.4	443	13	87	73	133	1.1	0.90
WSA21	2.4	35	106	2.1	88	40	142	56	72	0.3	0.91
WSA17	2.2	37	80	1.4	227	17	90	83	80	0.5	0.90
SHA1/15	1.0	26	52	2.6	366	15	105	145	102	0.5	0.90
SHA1/17	1.1	34	50	1.3	350	22	51	192	173	0.7	0.91
WSA12A	1.8	22	78	0.9	163	14	132	81	76	0.3	0.91
SHA1/20	0.7	21	51	0.9	204	12	36	70	26	0.4	0.92
WSA5A	1.1	21	85	2.1	256	29	109	89	85	0.3	0.91
SHA1/26	0.7	24	59	6.3	146	16	103	100	64	0.4	0.93
WSA3	1.4	25	68	1.2	238	25	50	119	149	0.4	0.92
SHA1/30	1.2	27	93	2.0	360	29	95	119	86	0.3	0.94
WSA2A	1.0	22	72	1.6	226	30	66	142	264	0.3	0.93
WSA2	1.8	19	64	1.4	201	28	72	150	325	0.3	0.90
WSA1B	1.2	20	89	2.1	222	24	128	99	142	0.2	0.91
SHA1/32	1.0	49	99	1.6	370	23	791	66	39	0.5	0.91
WSA1	1.5	39	91	1.8	173	27	122	108	148	0.4	0.91
SHA1/36	1.6	29	70	15.1	386	33	155	145	256	0.4	0.89

Table S3

Model reservoirs

Reservoir	Initial size	Description
Atmosphere		
CO_2	eqb[a]	Atmospheric CO_2
Ocean		
$DIC_{(s,h,d)}$	eqb[a]	Total carbon
$Alk_{(s,h,d)}$	eqb[a]	Total alkalinity
$O_{2(s,h,d)}$	eqb[a]	Oxygen
$PO_{4(s,h,d)}$	2.15 µM / kg-sw	Phosphate
$SO_{4(s,h,d)}$	28 mM / kg-sw	Sulfate
$H_2S_{(s,h,d)}$	0	Sulfide
Ca	10.28 mM / kg-sw	Calcium (single reservoir)

[a] set by initial spin-up to steady-state.

Table S4

Model fluxes, constants, and forcings.

Flux	Model Parameter	Value	Units	Description
crust/mantle				
f_{ccdeg}	k_{12_ccdeg}	varies[a]	mol CO_2 yr^{-1}	Degassing
land surface				
f_{carbw}	k_{14_carbw}	$1.33x10^{13}$	mol $CaCO_3$ yr^{-1}	Carbonate weatherability
f_{silw}	k_{silw}	varies[a]	mol "$CaSiO_3$" yr^{-1}	Silicate weatherability
f_{oxidw}	k_{17_oxidw}	varies[a]	mol C yr^{-1}	Oxidative weathering
f_{locb}	k_{5_locb}	$5x10^{12}$	mol C yr^{-1}	Land organic carbon burial
marine				
	$k_{O\_Asurf(s)}$	$0.85x3.6\ x10^{14}$	m^2	Ocean surface area
	$k_{O\_Asurf(h)}$	$0.15x3.6\ x10^{14}$		
	$k_{O\_vol(s)}$	$3.06\ x10^{16}$	m^3	Ocean volume
	$k_{O\_vol(h)}$	$1.35\ x10^{16}$		
	$k_{O\_vol(d)}$	$1.60\ x10^{21}$		
T	k_{O_circT}	20	Sv	Overturning circulation
f_{hd}	$k_{O\_circfhd}$	60	Sv	High latitude – deep exchange
	k_{piston}	0.3	m d^{-1}	Air-sea piston velocity
	$T_{O(s)}$	T_{mean}+ 6.5		Ocean temperature
	$T_{O(d)}$	max(T_{mean}-12.5,2.5)		
	k_{O_sal}	35	psu	Ocean salinity
	$r_{c:p}$	161		Redfield C:P ratio
	$r_{n:p}$	16		Redfield N:P ratio
f_{mccb}	$k_{carbsedshallow}$	varies[a]	mol $CaCO_3$ yr^{-1}	Marine carbonate burial
f_{mocb}	k_{2_mocb}	$5x10^{12}$	mol C yr^{-1}	Marine organic carbon burial

[a] parameters k_{silw}, k_{12_ccdeg}, $k_{carbsedshallow}$ are per-scenario external forcings.

Table S5 Biogeochemical processes

Flux	Biogeochemical transformation	Stoichiometry								Rate	Description
		$CO_{2(a)}$	DIC	Ca	O_2	P	H_2S	SO_4^{2-}	Alk		
	land surface										
f_{carbw}	$CO_2 + H_2O + CaCO_3 \rightarrow Ca^{2+} + 2HCO_3^-$	-1	2	1					2	Equation (S2)	Carbonate weathering
f_{silw}	$2CO_2 + H_2O + CaSiO_3 \rightarrow SiO_2 + Ca^{2+} + 2HCO_3^-$	-2	2	1					2	Equation (S1)	Silicate weathering
f_{oxidw}	$CH_2O + O_2 \rightarrow CO_2 + H_2O$	1	0	0					0	k_{17_oxidw}	Oxidative weathering
f_{locb}	$CO_2 + H_2O \rightarrow CH_2O + O_2$	-1	0	0					0	k_{5_locb}	Organic carbon burial
	marine										
f_{exp}	$CO_2 + H_2O + xP \rightarrow CH_2OP_x + O_2$		-1	0	$1+2r_{n:p}/r_{c:p}$	$-1/r_{c:p}$	0	0	$r_{n:p}/r_{c:p}$ [a]	see Section 3.2.4	Export production
	$CH_2OP_x + O_2 \rightarrow CO_2 + H_2O + xP$		1	0	$-1-2r_{n:p}/r_{c:p}$	$1/r_{c:p}$	0	0	$-r_{n:p}/r_{c:p}$ [a]	see Section 3.2.4	Aerobic remineralisation
	$CH_2OP_x + \frac{1}{2}SO_4^{2-} \rightarrow HCO_3^- + xP + \frac{1}{2}H_2S$		1	0	0	$1/r_{c:p}$	0.5	-0.5	1	see Section 3.2.4	Sulfate reduction
	$H_2S + 2O_2 \rightarrow SO_4^{2-} + 2H^+$		0	0	-2	0	-1	1	-2	see Section 3.2.4	Sulfide oxidation
f_{mccb}	$Ca^{2+} + HCO_3^- \rightarrow H^+ + CaCO_3$		-1	-1	0	0	0	0	-2	$k_{carbsedshallow}$	Carbonate

									$x(\Omega_{aragonite}-1)^{1.7}$	deposition
	$2H_2S + Fe(OH)_3 \rightarrow FeS_2 + \frac{1}{2}H_2 + 3H_2O$	0	0	-0.5	0	-2	0	0		Pyrite formation and burial
f_{mocb}	$CO_2 + H_2O \rightarrow CH_2O + O_2$	-1	0	1	0	0	0	0	k_{2_mocb}	Organic carbon burial

[a] contribution from nitrate, assumed at Redfield ratio.

Table S6

Steady-state initial conditions summary

	CO_2*Hi*	**CO_2*Lo***	**Units**	**Description**
Parameters				
k_{12_ccdeg}	11.80×10^{12}	11.80×10^{12}	mol CO_2 yr^{-1}	degassing
k_{17_oxidw}	5×10^{12}	5.92×10^{12}	mol C yr^{-1}	oxidative weathering
k_{silw}	2.40×10^{12}	6.60×10^{12}	mol $CaSiO_3$ yr^{-1}	Silicate weatherability
$k_{carbsedshallow}$	18.43×10^{12}	1.44×10^{12}	mol $CaCO_3$ yr^{-1}	Marine carbonate burial efficiency
Steady-state conditions				
pCO_2, ppm	2800	845		
T_{mean}	22.18	14.94	^0C	Global mean temp
$T_{O(s)}$	28.7	21.44	^0C	Ocean temp
$\Omega_{arag(s)}$	2.44	6.15		Aragonite saturation, ‘s’ box
pH	7.51,7.46,7.07	8.02, 7.99, 7.60	Total scale	Ocean pH, ‘s’,’h’,’d’
Alk total	5.28×10^{18}	6.07×10^{18}	mol	

DIC total	5.53×10^{18}	6.01×10^{18}	mol	
$\delta^{13}DIC_{(s)}$	+3.32	+2.97	‰	
Fluxes				
f_{carbw}	27.46×10^{12}	15.58×10^{12}	mol $CaCO_3$ yr^{-1}	Carbonate weathering
f_{silw}	6.80×10^{12}	7.72×10^{12}	mol "$CaSiO_3$" yr^{-1}	Silicate weathering
f_{ccdeg}	11.80×10^{12}	11.80×10^{12}	mol CO_2 yr^{-1}	Degassing
f_{mccb}	34.26×10^{12}	23.30×10^{12}	mol $CaCO_3$ yr^{-1}	Marine carbonate burial

Table S7

Overview of scenarios

Event	**Time**	**Scenario**	
		CO_2*Hi*	**CO_2*Lo***
		$\delta^{11}B_{sw}$=36.86	$\delta^{11}B_{sw}$=34
pH rise	252.25 Ma	Marine productivity increase	
	252.05 Ma	Carbonate sedimentation efficiency decrease	
		Pyrite deposition, Carbonate weathering increase	
$\delta^{13}C$ drop, stable pH	252.00 Ma	Land organic carbon burial decrease	
	251.95 Ma	Slow (~50kyr) isotopically light carbon addition.	
Acidification, no $\delta^{13}C$ change	251.88 Ma	Rapid (10kyr) isotopically heavy carbon addition	

Table S8 Sensitivity study for pH rise mechanisms. Perturbations applied to steady-state *CO_2Lo* at 252.05Ma, effect shown at 251.95Ma.

Mechanism	**Perturbation**	**$pH_{tot(s)}$**	**$\delta^{11}B_{(s)}$**	**$\Omega_{arag(s)}$**	**pCO_2**	**T_{mean}**	**Comments**
steady-state CO_2Lo	none	8.02	11.83	6.15	845	14.94	
		Δ	**Δ**	**Δ**	**Δ**	**Δ**	
'calc eff' decrease	$k_{carbsedshallow}$ $14.4x10^{11}$ → $2.47x10^{11}$ (ie x 0.17)	+0.266	+2.72	+5.55	-351	-2.58	
	$k_{carbsedshallow}$ $14.4x10^{11}$ → $1.23x10^{11}$ (ie x 0.085)	+0.36	+3.78	+8.2	-446	-3.39	
pyr deposition	'x1': $1.25x10^{12}$ mol FeS_2 yr^{-1}	+0.083	+0.71	-0.03	-213	-1.39	
	'x2': $2.5x10^{12}$ mol FeS_2 yr^{-1}	+0.155	+1.36	+0.12	-347	-2.46	
	'x4': $5x10^{12}$ mol FeS_2 yr^{-1}	+0.318	+3.062	+0.46	-557	-4.66	~ upper limit from Fe availability
carb input	'+1x': add $15x10^{12}$ mol $CaCO_3$ yr^{-1}	+0.082	+0.77	+1.44	-130	-0.81	+1x = approx 2x background weathering rate. Ocean carb deposition rapidly compensates
	'+2x': add $30x10^{12}$ mol $CaCO_3$ yr^{-1}	+0.147	+1.41	+2.76	-219	-1.44	+2x = ~3x background weath rate
	'+3x': add $45x10^{12}$ mol $CaCO_3$ yr^{-1}	+0.20	+1.97	+3.99	-285	-1.94	+3x = ~4x background weath rate
silw weath increase	x2 k_{silw} $6.60x10^{12}$→ $13.2x10^{12}$	+0.14	+1.19	+0.35	-329	-2.30	'Weatherability': drives pH primarily via pCO2 decrease

	x4 k_{silw} $6.60 \times 10^{12} \rightarrow 26.4 \times 10^{12}$	+0.32	+3.08	+0.57	-588	-5.09	
calc eff + pyr	$k_{carbsedshallow}$ 14.4×10^{11} -> 2.47×10^{11} 'x1': 1.25×10^{12} mol FeS_2 yr^{-1}	+0.37	+3.91	+5.78	-501	-3.98	used for Scenario *CO_2Lo*.
carb + pyr	'+2x': add 30×10^{12} mol $CaCO_3$ yr^{-1} 'x2': 2.5×10^{12} mol FeS_2 yr^{-1}	+0.28	+3.09	+2.92	-485	-3.79	

Table S9

Summary of pH rise mechanisms included in scenarios *CO_2Hi* and *CO_2Lo*

	Start Time	***CO_2Hi***	***CO_2Lo***
Productivity, anoxia	252.25 – 252.05Ma	Increase ocean P to 2.3x initial value (linear increase over 252.25 - 252.05Ma)	
Decrease in calcification effectiveness	252.05Ma	$k_{carbsedshallow}$ decrease from 1.8433×10^{13} to 0.72×10^{12}	$k_{carbsedshallow}$ decrease from 1.44×10^{12} to 2.47×10^{11}
Pyrite burial	252.05Ma	1.25×10^{12} mol FeS_2 yr^{-1}	
Carbonate weathering	251.95Ma	9.7×10^{12} mol/yr	

Table S10

Carbon injection perturbations, constrained to result in δ13Ccarb = -3 ‰ when applied to steady-state condition *CO_2Lo*

Size (mol C)	Duration	Rate (mol / yr)	$\delta^{13}C_{inj}$	Δ pH
4.75×10^{17}	10^5 yr	4.75×10^{12}	-50	-0.07
2.47×10^{18}	10^5 yr	2.47×10^{13}	-10	-0.28
3.32×10^{17}	10^4 yr	3.32×10^{13}	-50	-0.18
1.75×10^{18}	10^4 yr	1.75×10^{14}	-10	-0.64